Large Eddy Simulations of a Reverse Flow Combustion System

by

Jeffrey Spencer

A Thesis Presented in Partial Fulfillment
of the Requirements for the Degree
Master of Science

Approved March 2012 by the
Graduate Supervisory Committee:

Marcus Herrmann, Chair
Kangping Chen
Ronald Adrian

ARIZONA STATE UNIVERSITY

May 2012

ABSTRACT

Next generation gas turbines will be required to produce low concentrations of pollutants such as oxides of nitrogen (NO_x), carbon monoxide (CO), and soot. In order to design gas turbines which produce lower emissions it is essential to have computational tools to help designers. Over the past few decades, computational fluid dynamics (CFD) has played a key role in the design of turbomachinery and will be heavily relied upon for the design of future components. In order to design components with the least amount of experimental rig testing, the ensemble of sub-models used in simulations must be known to accurately predict the component's performance.

The present work aims to validate a CFD model used for a reverse flow, rich-burn, quick quench, lean-burn combustor being developed at Honeywell. Initially, simulations are performed to establish a baseline which will help to assess impact to combustor performance made by changing CFD models. Rig test data from Honeywell is compared to these baseline simulation results. Reynolds averaged Navier-Stokes (RANS) and Large Eddy Simulation (LES) turbulence models are both used with the presumption that the LES turbulence model will better predict combustor performance. One specific model, the fuel spray model, is evaluated next. Experimental data of the fuel spray in an isolated environment is used to evaluate models for the fuel spray and a new, simpler approach for inputting the spray boundary conditions (BC) in the combustor is developed. The combustor is simulated once more to evaluate changes from the new fuel spray boundary conditions. This CFD model is then used in a predictive simulation of eight other combustor configurations. All computer simulations in this work were preformed with the commercial CFD software ANSYS FLUENT.

NO_x pollutant emissions are predicted reasonably well across the range of configurations tested using the RANS turbulence model. However, in LES, significant under predictions are seen. Causes of the under prediction in NO_x concentrations are investigated. Temperature metrics at the exit of the combustor, however, are seen to be better predicted with LES.

ACKNOWLEDGEMENTS

I would like to thank Marcus Herrmann and Sunil James for their guidance through this project. I would also like to thank Honeywell for funding this project, as well as all the others at Honeywell that were involved in this work.

TABLE OF CONTENTS

CHAPTER Page

LIST OF FIGURES

Figure Page

Figure Page

Figure Page

Figure Page

Figure Page

LIST OF SYMBOLS

$[i]$	Concentration of species i
χ	Scalar dissipation rate
δ_{ij}	Kronecker delta
$\dot{m}$	Mass flow rate
ε	Dissipation rate
Λ	Wavelength of the fastest growing wave
λ	Thermal conductivity
$\mathfrak{D}$	Mass diffusion coefficient
μ	Dynamic viscosity
ν_t	Turbulent viscosity or eddy viscosity
ω_i	Reaction rate
Φ	Arbitrary quantity
ρ	Gas phase density
ρ_l	Fuel density
σ_k	Turbulent Prandtl for k
σ_ε	Turbulent Prandtl for ε
τ	Breakup time
τ_{ij}	Deviatoric stress tensor or viscous stress tensor

τ_{ij}^{SGS} Subgrid scale stress tensor

$\mathbf{U}_p$ Droplet velocity

$\mathbf{x}_p$ Droplet position

Θ_{eq} Characteristic angle of an equilateral cell

Θ_{max} Maximum angle between faces of element

Θ_{min} Minimum angle between faces of element

$\forall$ Volume

a Parent droplet radius

B_0 WAVE model constant

B_1 WAVE model constant

c_p Specific heat

C_s Smagorinsky SGS model constant

$C_{\varepsilon 1}$ k-ε model constant

$C_{\varepsilon 2}$ k-ε model constant

C_g Variance of mixture fraction model constant

C_u k-ε model constant

C_{var} LES variance model constant

D Drop diameter

D_p Inverse of droplet relaxation timescale

FN_{US}	Flow number
k	Kinetic energy
k_f	Forward reaction rate
k_r	Backward reaction rate
Le	Lewis number
M_i	Molecular weight of species i
p	Pressure
Q	Cumulative volume fraction
q	Rosin Rammler (RR) spread
r	Child droplet radius
Re	Reynolds number
S_{ij}	Strain rate tensor or rate of deformation tensor
SMD	Sauter Mean Diameter
T	Temperature
t	Time
U	Velocity
X	Characteristic diameter
x	Coordinate direction
Y_i	Mass fraction of species i

Z	Mixture fraction
Z''	Mixture fraction variance

Chapter 1

Introduction

1.1 Background

As the technology of gas turbines progresses and concern about the pollutants these machines create increases, there is more pressure to decrease emission levels. The combustor, a component of a gas turbine engine which primarily controls the levels of pollutants, accepts air from the compressor, reacts a portion of the air with fuel, and sends the hot gases through a turbine. Combustors come in a few geometry styles such as can, can-annular, and annular. The combustor studied here is an annular combustor from an aircraft Auxiliary Power Unit (APU) currently being developed by Honeywell. APUs are found on most aircraft and are used for purposes other than propulsion. There are two types of combustor flow designs: straight through and reverse flow. The reverse flow combustor investigated in this study uses a technology known as rich-burn, quick-quench, lean-burn (RQL) to reduce concentrations of NOx. NOx is largely formed in flames that are near stoichiometric. Therefore, this technology aims to avoid stoichiometric mixtures by burning the fuel rich in the primary zone and then quickly mixing the products with air to a temperature that is low enough that little NOx is formed but high enough that reactions such as the oxidation of CO and soot can continue. This path of low NOx production is shown in Figure 1.1.

Today's computational resources allow combustion engineers to accelerate the design process and decrease the number of configurations that need to be tested. Thus it is important that a CFD code is able to predict changes in combustor performance from one combustor configuration to another. Although computational power is always increasing, currently it is not practical to resolve the smallest scales found in the flow of a complex combustor. Therefore, physical models are used for

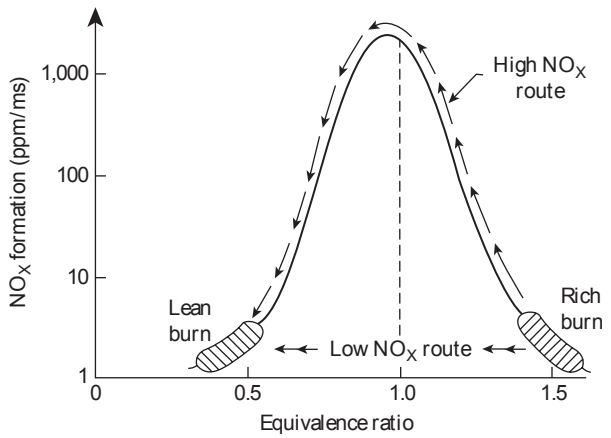

Figure 1.1: Drawing illustrating the RQL concept [1].

the physics that is not resolved by the computational mesh such as turbulence, the atomization of the fuel, and combustion.

1.2 Objective and Overview

The overall objective of this work is to develop a CFD method to accurately predict the performance of a reverse flow combustor by validating the model for three combustor configurations. Models used to describe atomization are evaluated since combustor simulations are known to be sensitive to fuel boundary conditions. Initial simulations were performed using an industry best practice approach for the fuel spray boundary conditions. Simulation results were then compared to rig test data made available by Honeywell. An evaluation of the accuracy of the fuel spray model was then performed. Experimental results of the atomizer in a pressure chamber were used to develop and validate a method of prescribing the boundary conditions and models used for the fuel spray. Simulations of the combustors were then run again using the new fuel spray boundary conditions. Additional to the fuel spray model, adjustments to the initial set of submodels were also made and will be discussed later.

The combustor geometries and pressure chamber geometries used for the spray modeling were previously defined and were meshed using the commercial software, Gambit (v2.3.16). The commercial software, ANSYS FLUENT (v12.0.16 and v13.0.0), was used for the computer simulations.

Chapter 2

Baseline Combustor Simulations

2.1 Setup

A 36 degree sector with an atomizer located in the center of the sector was meshed since the entire combustor contains 10 fuel nozzles and the periodicity of the combustor can be taken advantage of. The combustor as well as the annulus was simulated. Simulating the combustor annulus as well as the combustor simplifies the boundary conditions since the boundary conditions for the liner effusion cooling holes and dilution air holes do not need to be specified and instead mass flow rates through these holes become part of the solution. Figure 2.1 shows a sector of one of the combustor configurations. Fuel is introduced into each combustor configuration through the same pressure atomizer for each configuration. This atomizer is surrounded by an air swirler whose geometry, such as angle and diameter of the holes, differs among the three configurations. Table 2.1 lists the 3 configurations and shrouds used in each configuration. The swirler geometries are shown in Figure 2.2. The fluid geometry was meshed using a hybrid of hexahedral and tetrahedral cells. The three configurations were each meshed with approximately 12.5 million cells. Care was taken to avoid excessively skewed cells, which is defined in Gambit as having a skewness greater than 0.97. A majority of the cells retained a skewness of less than 0.90. Skewness is a metric used to judge the quality of a hexahedral or tetrahedral and is calculated from angles, Θ, within the mesh cell. It is defined as,

$$Skewness = max\left[\frac{\Theta_{max}-\Theta_{eq}}{180-\Theta_{eq}}, \frac{\Theta_{eq}-\Theta_{min}}{\Theta_{eq}}\right]. \tag{2.1}$$

Θ_{eq} is 60 degrees for tetrahedral cells and 90 for hexahedral cells.

The effusion cooling holes are very small in size compared to dimensions of the combustor which would lead to a very large mesh cell count if a continuous mesh was used. Non-conformal interfaces are used to circumvent this problem. Non-conformal interfaces do not need to have connected nodes and therefore the mesh can transition from small to large cells instantaneously, however, the solution will not be accurate around these regions. Figure 2.3 shows an example of a non-conformal mesh.

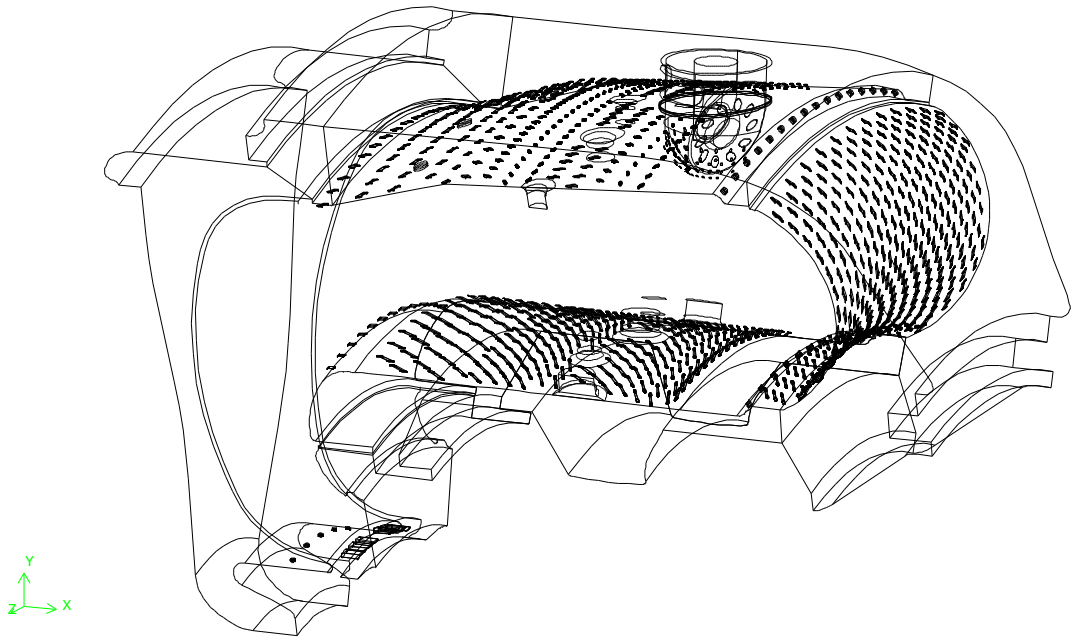

Figure 2.1: 3D view of a representative geometry of one of the combustor configurations.

Boundary conditions to the CFD model were supplied by Honeywell. Figure 2.4 shows a cross section of the combustor labeled with the following discussed boundary conditions. The inlet of the combustor is supplied air through a set of vanes. The direction of the air is specified by the geometry of these vanes. The mass flow rate of the air and the temperature of the air are also inputs. A pressure outlet boundary

Table 2.1: Changes among the baseline configurations.

Test	Swirlers	Quench Holes	Effusion	Secondary Air		Comment
				Inner	Outer	
Test 3a	S3a	Q3abc	E3abc	None	SAO3abc	
Test 3b	S3b	Q3abc	E3abc	None	SAO3abc	
Test 3c	S3c	Q3abc	E3abc	None	SAO3abc	

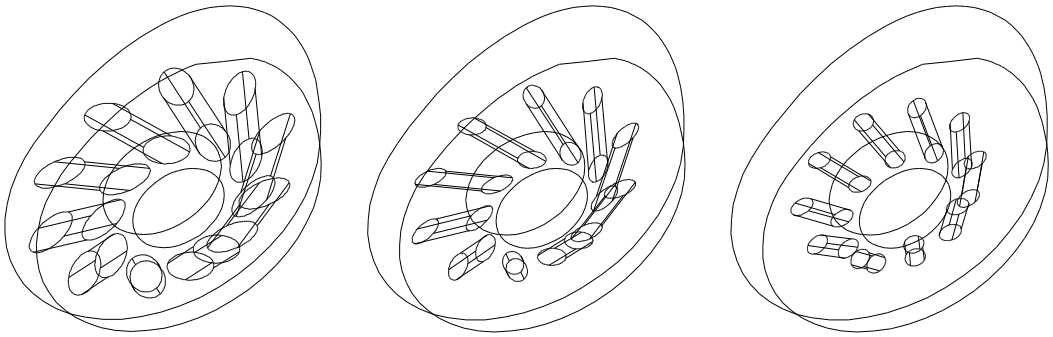

(a) S3a (b) S3b (c) S3c

Figure 2.2: Swirler geometries which enclose the atomizer.

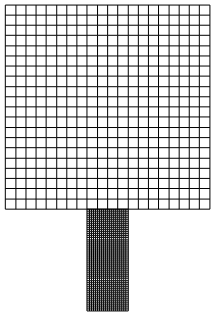

Figure 2.3: Illustration of a non-conformal mesh interface.

condition is assigned at the exit of the combustor based upon the operating pressure of the combustor. In addition to the combustor exit, air also exits the annulus at three additional locations, known as bleeds. The mass flow rate out of these exits is known but these boundary conditions were converted to prescribed velocity normal to the exit surface due to difficulties running the simulations. Temperatures found

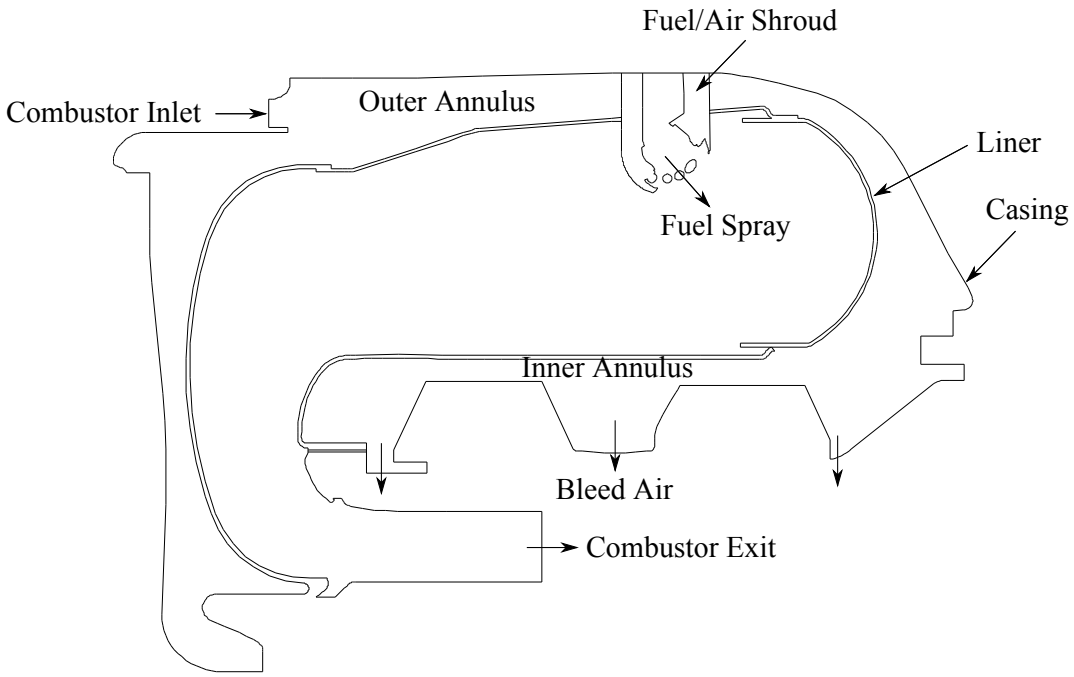

Figure 2.4: 2D cross section of one of the combustor configurations.

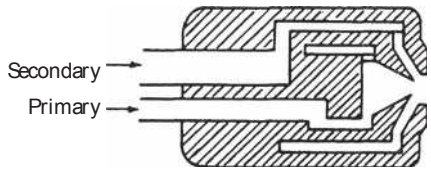

Figure 2.5: Cross section of a dual orifice atomizer [2].

in rig tests are used to assign liner wall temperatures for most of the simulations, however, using adiabatic walls was shown in one instance to improve the accuracy of NO_x prediction. The casing walls are given adiabatic boundary conditions.

This combustor uses a dual orifice pressure atomizer to supply Jet A, aviation fuel. A cross section of the basic design of this type of atomizer is shown in Figure 2.5. The atomizer as well as atomization models will be discussed in more detail in Chapter 3 but the fuel boundary conditions for the baseline simulations will be discussed here. The pressure differential of the atomizer is measured in the rig and

the mass flow rate of the fuel can be calculated from this pressure differential and the flow number, which is a property of the atomizer. The flow number is given as,

$$FN_{US} = \frac{\dot{m}}{\Delta p^{1/2}}. \tag{2.2}$$

From Bernoulli's equation, the velocity of the fuel exiting the atomizer can be calculated,

$$U = \sqrt{\frac{2\Delta p}{\rho_l}}. \tag{2.3}$$

The fuel is injected as spherical droplets in the shape of a cone with a SMD given from experimental data. The SMD is obtained using a Malvern particle sizer. There are a few mathematical functions to describe a drop size distribution. One of the most common methods is that of Rosin and Rammler [3]. The diameters of the droplets are determined from a Rosin-Rammler function,

$$1 - Q = exp\left(-\frac{D}{X}\right)^q. \tag{2.4}$$

From equations given by Lefebvre [2] that relate X and the Sauter mean diameter (SMD), an equation can be used to input a range of diameters with desired diameter distribution,

$$Q = 1 - exp\left(-\Gamma\left[1 - \frac{1}{q}\right]^{-q}\left[\frac{D}{SMD}\right]^q\right). \tag{2.5}$$

The SMD and Rosin-Rammler spread (q) are obtained experimentally. The Sauter mean diameter is a type of mean droplet diameter that is often used in combustion applications and is given by the ratio of the volume of the droplets and surface area of the droplets in the spray.

The boundary conditions are labeled in Gambit but values are assigned in ANSYS FLUENT. Once the mesh for fluid geometry had been generated using Gambit,

the mesh was exported to be read into ANSYS FLUENT and these boundary conditions are assigned. Next, the models for the physics in the combustor such as turbulence, combustion, pollution formation, and the fuel spray will be discussed.

2.2 CFD Models

2.2.1 Turbulence

First, the governing equations for the flow of fluids must be reviewed before models for turbulence are discussed. Index notation is used in the following equations. In this notation, the momentum equation represents an equation in each coordinate direction and repeated indices are summed for the three directions. The continuity and Navier-Stokes equations for the gas phase are as followed,

$$\frac{\partial \rho}{\partial t} + \frac{\partial (\rho U_i)}{\partial x_i} + Sources = 0, \tag{2.6}$$

$$\frac{\partial (\rho U_i)}{\partial t} + \frac{\partial (\rho U_j U_i)}{\partial x_j} = -\frac{\partial p}{\partial x_i} + \frac{\partial \tau_{ij}}{\partial x_j} + Sources. \tag{2.7}$$

The sources in the equations above come from the liquid fuel spray. As fuel evaporates, mass is added to the continuity equation for the gas phase above. Similarly, momentum is exchanged between the gas phase and liquid fuel spray and is accounted for with the inclusion of the source term in the momentum equation for the gas phase above.

This now leads to the discussion of turbulence models. The scales encountered in the flow range from the integral length scale which is proportional to the geometry of the combustor, down to the Kolmogorov scales which are the smallest scales in the flow. Resolving all the scales is known as Direct Numerical Simulation (DNS). For DNS, the number of grid points for resolving all scales needs to be of the order $Re^{9/4}$[4] and due to limitations in computing power, this limits the highest

Reynolds number that can be used in a simulation, which makes DNS of a complex, realistic combustor almost impossible with today's computational resources. Alternatively, the Navier-Stokes equations can be time averaged to obtain only the mean fields. This turbulence model is known as Reynolds averaged Navier-Stokes (RANS). Averaging the Navier-Stokes equation introduces an extra term that cannot be explicitly computed, the Reynolds stress. There are many methods to go about modeling this term but all of these methods have constants that need to be tuned for different flow conditions. This usually requires experimental data in order to tune the model constants, which is very inconvenient in many situations. A method that fits in between these two computational methods is Large Eddy Simulations (LES). In this type of computation the large scales are computed exactly (resolved) and the small scales are left unresolved and are modeled. This method seems logical since most of the kinetic energy is in the large scales. Since the turbulence approaches isotropy as the length scale decreases, the small scales should be easier to model universally. Although the mesh requirements are not as stringent as DNS, LES still requires great amounts of computational resources.

The first turbulence model used for this work is the RANS turbulence model. In non-reacting flows, the traditional method to arrive at this turbulence model is to first Reynolds decompose the velocity fields, meaning that the velocity is split into a time average component and a fluctuating component like so: $U = \overline{U} + u'$, where $\overline{u'} = 0$. A time average of a quantity is defined as,

$$\overline{\Phi} = \lim_{\Delta t \to \infty} \frac{1}{\Delta t} \int_{t_0}^{t_0+\Delta t} \Phi \, dx. \tag{2.8}$$

However, since the density varies in reacting flows, the velocity fields are decomposed using a Favre averaged quantity and a fluctuating component like so:

$U = \widetilde{U} + u''$ where $\overline{u''} \neq 0$ but $\overline{\rho u''} = 0$. The Favre average for some quantity, Φ, is defined as,

$$\widetilde{\Phi} = \frac{\overline{\rho\Phi}}{\overline{\rho}}. \tag{2.9}$$

The velocity fields are decomposed using Favre averages and Reynolds decomposition is used for ρ and p. The continuity and momentum equations are then time averaged. Note that time averaging commutes with differentiation and additive terms can be separately time averaged. For example,

$$\overline{\frac{\partial U}{\partial x_i}} = \frac{\partial \overline{U}}{\partial x_i}$$

$$\overline{\overline{U} + u'} = \overline{\overline{U}} + \overline{u'} = \overline{U} + \cancelto{0}{\overline{u'}}$$

The averaged Navier-Stokes are as followed,

$$\frac{\partial \overline{\rho}}{\partial t} + \frac{\partial (\overline{\rho}\widetilde{U_i})}{\partial x_i} + Sources = 0, \tag{2.10}$$

$$\frac{\partial (\overline{\rho}\widetilde{U_i})}{\partial t} + \frac{\partial (\overline{\rho}\widetilde{U_j}\widetilde{U_i})}{\partial x_j} + \frac{\partial (\overline{\rho u_j'' u_i''})}{\partial x_j} = -\frac{\partial \overline{p}}{\partial x_i} + \frac{\partial \overline{\tau_{ij}}}{\partial x_j} + Sources. \tag{2.11}$$

Newton's viscosity law is used to represent the deviatoric stress tensor,

$$\tau_{ij} = -\frac{2}{3}\mu \frac{\partial U_k}{\partial x_k} \delta ij + 2\mu S_{ij}, \tag{2.12}$$

where,

$$S_{ij} = \frac{1}{2}\left[\frac{\partial U_i}{\partial x_j} + \frac{\partial U_j}{\partial x_i}\right]. \tag{2.13}$$

Equation (2.12) is time averaged and the velocity decomposed using Favre averages. The final form of the averaged momentum equation is obtained,

$$\frac{\partial(\overline{\rho}\widetilde{U_i})}{\partial t}+\frac{\partial(\overline{\rho}\widetilde{U_j}\widetilde{U_i})}{\partial x_j}+\frac{\partial(\overline{\rho}\widetilde{u_j''u_i''})}{\partial x_j}=-\frac{\partial\overline{p}}{\partial x_i}+\frac{\partial\overline{\tau_{ij}}}{\partial x_j}+Sources. \tag{2.14}$$

The two equations averaged using Favre averages turn out to be similar in form to the traditional Reynolds averaged Navier-Stokes equations. This equation is unclosed due to the third term on the right. This term is known as the Reynolds stress and needs to be modeled. This is accomplished through the gradient transport approximation,

$$\overline{\rho}\widetilde{u_i''u_j''}=-\overline{\rho}\nu_t\left[2\widetilde{S_{ij}}-\frac{2}{3}\delta_{ij}\frac{\partial\widetilde{U_k}}{\partial x_k}\right]+\frac{2}{3}\delta_{ij}\overline{\rho}k. \tag{2.15}$$

To obtain the turbulent viscosity, ν_t, a two equation, k-ε closure model is used. In this model, two additional equations, one for the kinetic energy and the other for the dissipation rate, are solved for. The turbulent viscosity is then found from the equation,

$$\nu_t=C_u\frac{k^2}{\varepsilon}. \tag{2.16}$$

An equation for the kinetic energy can be found by taking the dot product of the momentum equation with velocity. An equation for the dissipation rate, ε, can be derived from the Navier-Stokes by taking the derivative; however, this equation for the dissipation rate has many terms that need to be modeled. Alternatively, a model equation for ε is found by multiplying the k equation by ε/k. The two equations

can be found throughout literature as [6],

$$\frac{\partial(\overline{\rho}k)}{\partial t}+\frac{\partial(\overline{\rho}\widetilde{U_j}k)}{\partial x_j}=\frac{\partial}{\partial x_j}\left[\left(\mu+\frac{\mu_t}{\sigma_k}\right)\frac{\partial k}{\partial x_j}\right]-\overline{\rho}\widetilde{u_i''u_j''}\frac{\partial\widetilde{u_i}}{\partial x_j}-\overline{\rho}\varepsilon + Sources, \quad (2.17)$$

$$\frac{\partial(\overline{\rho}\varepsilon)}{\partial t}+\frac{\partial(\overline{\rho}\widetilde{U_j}\varepsilon)}{\partial x_j}=\frac{\partial}{\partial x_j}\left[\left(\mu+\frac{\mu_t}{\sigma_\varepsilon}\right)\frac{\partial\varepsilon}{\partial x_j}\right]-C_{\varepsilon1}\frac{\varepsilon}{k}\left(\overline{\rho}\widetilde{u_i''u_j''}\frac{\partial\widetilde{u_i}}{\partial x_j}\right)-C_{\varepsilon2}\overline{\rho}\frac{\varepsilon^2}{k} + Sources. \quad (2.18)$$

A modified form of this turbulence model known as the realizable k-ε model [7] is used for this work where Equation (2.16) is reformulated in a realizable form and the equation for the rate of dissipation is derived from the dynamic equation of the mean-square vorticity formation at large Reynolds number. Although it is very common to tune the turbulence model constants for a specific flow condition, it should be noted that the constants for this model have not been tuned for this configuration and default values in ANSYS FLUENT are used.

The next turbulence model used is the LES turbulence model. As previously stated, in this model the larger scales are resolved or computed and the smaller scales are modeled. The grid acts as a filter and therefore the size of the smallest resolved scale is proportional to the grid size. Here the operator $\overline{*}$ now represents the spatial filtering and quantities can be filtered to produce a resolved and unresolved quantity. For example: $U=\overline{U}+u'$. $\overline{U}$ is now known as the resolved quantity and u' is the subgrid quantity. The operator $\widetilde{*}$ still represents the Favre average. Equation (2.9) and $\overline{\rho u''}=0$ are still true with the new $\overline{*}$ operator. The governing equations for LES can be obtained by applying a filtering operation to the Navier-Stokes

equations. A vector or scalar quantity can be filtered as,

$$\overline{\Phi}(\mathbf{x},t) = \int G(\mathbf{x},\mathbf{y})\Phi(\mathbf{y},t)\,d\mathbf{y}. \tag{2.19}$$

The function G is the filter. The Navier-Stokes equations are filtered in a similar manner to how these equations were time averaged to obtain the RANS equations. The result is,

$$\frac{\partial \overline{\rho}}{\partial t} + \frac{\partial (\overline{\rho}\widetilde{U_i})}{\partial x_i} + Sources = 0, \tag{2.20}$$

$$\frac{\partial (\overline{\rho}\widetilde{U_i})}{\partial t} + \frac{\partial (\overline{\rho}\widetilde{U_j}\widetilde{U_i})}{\partial x_j} = -\frac{\partial \overline{p}}{\partial x_i} + \frac{\partial \widetilde{\tau_{ij}}}{\partial x_j} - \frac{\partial \tau_{ij}^{SGS}}{\partial x_j} + Sources. \tag{2.21}$$

Similarly to how the Reynolds stress came about in the RANS equations, there is an extra term in the filtered Navier-Stokes. This is the term, τ_{ij}^{SGS}, and is equal to. $\widetilde{U_iU_j} - \widetilde{U_i}\widetilde{U_j}$, and originates from the nonlinear convective term since $\widetilde{U_iU_j} \neq \widetilde{U_i}\widetilde{U_j}$. This term is called the residual stress tensor or the subgrid-scale (SGS) stress tensor. This term does not possess the same physical significance that the Reynolds stress term did. This term represents the effect that the small scales have on the large scales and is modeled. Understanding the interaction between the small scales and large scales, and modeling this term is of significant importance in LES. Development of more accurate models for this term is an active area of research. One of the most common and simplistic SGS stress models is that of Smagorinsky [8]. First, an eddy viscosity/Boussinesq's assumption is made so that the deviatoric (traceless) SGS stress tensor is,

$$\tau_{ij}^{SGS} - \frac{1}{3}\tau_{kk}^{SGS}\delta_{ij} = -2\nu_t\widetilde{S_{ij}}. \tag{2.22}$$

ν_t is of course different than that of the RANS model and using Smagorinsky's model it is modeled as,

$$\nu_t = (C_s \Delta x)^2 |\widetilde{S}|, \tag{2.23}$$

where $|\widetilde{S}| = (2\widetilde{S_{ij}}\widetilde{S_{ij}})^{1/2}$.

This model has been shown to be overly dissipative [9] and an improvement to this model can be made by dynamically computing the model constant, C_s. This model is known as the dynamic Smagorinsky model [10] and is the SGS stress model used in LES simulations of this work.

2.2.2 Combustion

The next model to be discussed is that for combustion. First, a brief explanation of the different combustion regimes is needed. Fuel burns in three types of combustion regimes: premixed, non-premixed, and partially premixed. Premixed combustion occurs when the oxidizer, for gas turbine combustors this is air, and fuel are mixed on a molecular level before being burnt. Partially premixed combustion is where fuel and oxidizer are imperfectly mixed prior to being burnt. Non-premixed or also called diffusion combustion occurs when fuel is not initially premixed but mixes with oxidizer after the fuel is introduced. In the case of liquid fuel, it must first evaporate and this vapor must mix with the gas phase where it can be burnt. Burning of liquid fuel results in partially premixed combustion since it is not completely non-premixed but is modeled with a non-premixed combustion model since partially premixed combustion premixed models are still an active area of research.

Assuming complete combustion, a 1 step, global chemical reaction such as,

$$\nu'_F C_m H_n + \nu'_{O_2} O_2 \rightarrow \nu''_{CO_2} CO2 + \nu''_{H_2O} H_2O, \tag{2.24}$$

where:

$$v'_F = 1;\ v'_{O_2} = m + \frac{n}{4};\ v''_{CO_2} = m;\ v''_{H_2O} = \frac{n}{2}, \tag{2.25}$$

describes the combustion of some single component, hydrocarbon fuel. This simple reaction is often too simplistic to describe the complex combustion of fuel. An improvement is to assume equilibrium and to take into account the dissociation of products by allowing backward reactions,

$$v'_F C_m H_n + v'_{O_2} O_2 \rightleftharpoons v''_{CO_2} CO_2 + v''_{H_2O} H_2O. \tag{2.26}$$

Using either a 1 step global reaction assuming complete combustion or chemical equilibrium, the species and temperatures of the fuel/oxidizer mixtures can be found to be functions of a variable known as the mixture fraction [11]. The mixture fraction for one fuel inlet/one oxidizer inlet systems is defined as,

$$Z = \frac{\dot{m}_{fuel}}{\dot{m}_{fuel} + \dot{m}_{ox}}, \tag{2.27}$$

where $\dot{m}_{fuel}$ is the mass flow rate of the fuel into the combustor and $\dot{m}_{ox}$ is the mass flow rate of the oxidizer into the combustor.

The mixture fraction is a conserved quantity and combustion models that use this approach are known as conserved scalar models. This type of combustion model is useful since it separates the computation of chemistry from the flow solution allowing chemistry tables to be computed prior to performing the solution of the flow. This allows for series of elementary reactions or reaction mechanisms to be used which can more accurately describe the complex reactions that occur with the combustion of fuels.

A common combustion model used in non-premixed combustion is the steady laminar flamelet model. This model is still based on fast chemistry but is able to account for non-equilibrium or straining effects through a variable known as the scalar dissipation rate. In this model the flame is viewed as a group of one dimensional laminar flames. A new coordinate system is defined that is normal to the mixture fraction variable. Similar to a boundary layer approximation, by assuming the gradients in the direction normal to the flame are much larger than in tangential directions, the flame structure can be viewed as being 1D. The time derivative only becomes important in situations of rapid changes such as ignition and extinction, which is not studied in this work. These 1D flames can be generated with a counterflow geometry where a flame is stabilized between two opposed tubes, one containing oxidizer and the other gaseous fuel. The strain rate or scalar dissipation rate is varied by changing the inlet velocity, resulting in scalar dissipation rates of approximately 0 s^{-1} until χ_q when the flame is extinguished. The equations for the species concentrations in mixture fraction space are described by the steady flamelet equations [11],

$$\rho \mathfrak{D} \left(\frac{dZ}{dx} \right)^2 \frac{d^2 Y_i}{dZ^2} + \omega_i = 0. \tag{2.28}$$

The derivation of these equations involves assuming the Lewis number of all species are equal to 1 (i.e. equal species diffusivity). The Lewis number is defined as,

$$Le_i = \frac{\lambda}{\rho \mathfrak{D}_i c_p}. \tag{2.29}$$

In Equation (2.28), the scalar dissipation rate can be defined as,

$$\chi = 2\mathfrak{D}\left(\frac{dZ}{dx}\right)^2. \tag{2.30}$$

The scalar dissipation rate is the only term that contains spatial derivatives from the flow solution.

An equation of the temperature of the oxidizer/fuel mixture is,

$$\rho\frac{\partial T}{\partial t} = \frac{\rho\chi}{2}\frac{\partial^2 T}{\partial Z^2} - \frac{1}{c_p}\sum_{i=1}^{n} H_i\omega_i + \frac{\rho\chi}{2c_p}\left[\frac{\partial c_p}{\partial Z} + \sum_{i=1}^{n} c_{p,i}\frac{\partial Y_i}{\partial Z}\right]\frac{\partial T}{\partial Z} \tag{2.31}$$

where changes in the spatial direction have been neglected since they are small compared to those in mixture fraction and the change of pressure in time is neglected since pressure does not vary much in time [12]. The equations describing the counter flow flame can be solved independently of the flow solution between the limits of mixture fraction (0 to 1) and between a range of scalar dissipation rates, given the initial temperatures of the oxidizer stream and temperature at which the liquid fuel vaporizes. These preprocessed solutions are known as flamelet libraries. The flamelet libraries for this work were generated from a detailed reaction mechanism containing 62 species, 344 elementary reaction mechanisms used to represent the Jet A fuel. Note, the flow solution will need to also solve an energy equation to describe the heat transfer to the liquid droplets and to/from the liner walls when non-adiabatic BCs are used.

To account for effects of turbulence, a presumed shape probability density function (PDF) is used. The beta PDF is used here,

$$P(Z) = \frac{Z^{\alpha-1}(1-Z)^{\beta-1}}{\int Z^{\alpha-1}(1-Z)^{\beta-1}dZ}, \tag{2.32}$$

where,

$$\alpha = \widetilde{Z}\left[\frac{\widetilde{Z}(1-\widetilde{Z})}{\widetilde{Z''^2}} - 1\right], \tag{2.33}$$

$$\beta = (1-\widetilde{Z})\left[\frac{\widetilde{Z}(1-\widetilde{Z})}{\widetilde{Z''^2}} - 1\right]. \tag{2.34}$$

The beta PDF is dependent on the first two moments of the mixture fraction, the mean mixture fraction and mixture fraction variance. In RANS, transport equations are solved for the mean mixture fraction and mixture fraction variance. The transport equation for the mixture fraction is,

$$\frac{\partial \overline{\rho}\widetilde{Z}}{\partial t} + \frac{\partial(\overline{\rho}\widetilde{U}_i\widetilde{Z})}{\partial x_i} = \frac{\partial}{\partial x_i}\left(\frac{\mu_t}{\sigma_t}\frac{\partial \widetilde{Z}}{\partial x_i}\right) + Sources, \tag{2.35}$$

where the source term is only due to mass transferred to the gas phase from the fuel (i.e. there are no chemical source terms). The transport equation for the mixture fraction variance is,

$$\frac{\partial \overline{\rho}\widetilde{Z''^2}}{\partial t} + \frac{\partial(\overline{\rho}\widetilde{U}_i\widetilde{Z''^2})}{\partial x_i} = \frac{\partial}{\partial x_i}\left(\frac{\mu_t}{\sigma_t}\frac{\partial \widetilde{Z''^2}}{\partial x_i}\right) + C_g\mu_t\left(\frac{\partial \widetilde{Z}}{\partial x_i}\right)^2 - \overline{\rho}\widetilde{\chi}. \tag{2.36}$$

In LES, the variance can be modeled as [13],

$$\widetilde{Z''^2} = C_{var}\Delta x^2 |\nabla \widetilde{Z}|^2. \tag{2.37}$$

When the PDF is convoluted with quantities from flamelet libraries, one is able to obtain density weighted mass fractions,

$$\widetilde{\Phi} = \int_0^1 \Phi(Z, \chi_{st}) P(Z; \widetilde{Z}, \widetilde{Z''^2})\, \mathrm{d}Z. \tag{2.38}$$

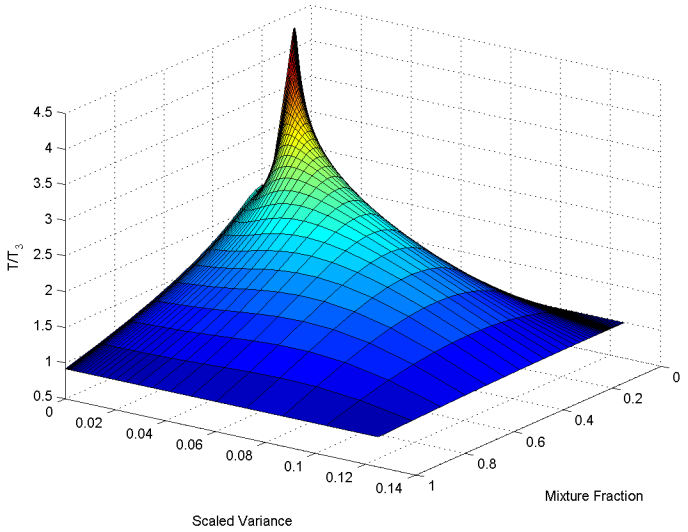

Figure 2.6: Favre averaged temperature table for a given scalar dissipation rate.

Preprocessed chemistry tables are computed as a result of this convolution. An example of preprocessed values for temperature for a given scalar dissipation rate is shown in Figure 2.6. The temperature is seen to reach a peak near stoichiometric conditions at a variance of 0. As the mixture fraction reaches 0, the mixture is pure oxidizer and is equal to the input temperature for the oxidizer. As the mixture fraction reaches 1, the mixture is pure fuel vapor and is equal to the input temperature for the point at which the fuel vaporizes. As the variance increases, the temperature decreases.

For all species and temperature of the mixture in the flamelet library, three dimensional chemistry tables were generated, with the temperature or species being functions of mixture fraction, mixture fraction variance and scalar dissipation rate. The process of generating chemistry tables is equally valid when using an equilibrium model except now the tables will be one less dimension since they do not depend on scalar dissipation rate.

2.2.3 *Fuel Spray*

The model for the fuel spray will now be discussed. If the volume loading of the fuel is low, the fuel spray can be modeled using point sources that are tracked as they move throughout the continuous gas phase. In this approach the gas phase is solved using the Navier-Stokes equations previously described and the droplets are tracked using a Lagrangian reference frame. To reduce the number of objects tracked, computational parcels are used. In this method, parcels are the objects tracked which contain a number of actual droplets of similar diameter and size. Mass and momentum are exchanged between the droplets and gas phase by source terms in the Navier-Stokes equations. A two way interaction or coupled method was used for all the spray models. This method accounts for forces from the gas phase that act upon the droplets as well as forces from the droplets acting upon the gas phase. The governing equations for the droplets, which are only acted on by drag forces, are [14],

$$\frac{d\mathbf{x}_p}{dt} = \mathbf{U}_p, \tag{2.39}$$

$$\frac{d\mathbf{U}_p}{dt} = D_p(\mathbf{U} - \mathbf{U}_p), \tag{2.40}$$

where the velocity vector is now written as $\mathbf{U}$ for the gas phase and $\mathbf{U}_p$ for the velocity of the droplets.

This coupled set of ordinary differential equations is solved for the locations of the droplets and their velocities. ANSYS FLUENT employs a series of laws governing the temperature of the droplets for specified ranges of droplet temperatures. When the temperature of the droplet is below the vaporization temperature, the temperature of the droplet is governed by a simple heat balance and the droplet

is only heated. When the temperature of the droplet is above the vaporization temperature but below the boiling point, the temperature is governed by a heat balance that takes into account the rate of evaporation of fuel to the gas phase. Another set of governing laws is applied if the temperature of the droplet is above the boiling point. Fuel vapor is added to the gas phase as droplets evaporate and the temperature of the droplets is governed by the heat balance that is appropriate for the range of temperatures the droplet is in.

As previously discussed, for these simulations the fuel is injected as spherical droplets in the shape of a cone for each orifice of the atomizer. The range of diameters is input from the SMD and Rosin-Rammler spread parameter used to describe a diameter distribution of a spray, Equation (2.5). The diameter distribution is already correct since it is input from experimental data and there is no need to include additional models, specifically secondary breakup models which will be discussed in Chapter 3.

2.2.4 NO_x

Oxides of nitrogen or NO_x are pollutants formed in the combustion of fuel. The reaction mechanism includes a set of reactions for the formation of NO_x, however, since the steady laminar flamelet model assumes fast chemistry, slow forming pollutants such as NO are not able to be predicted correctly. Therefore, a pollutant model for the prediction of NO_x is used. There are three main ways these pollutants are formed. The first formation method is thermal NO_x, which will be described in detail shortly. The second formation method is prompt formation. In this method radicals from the burning fuel combine with nitrogen to form nitrogen elements which combine with oxygen to form NO. The third formation method is fuel NO_x formation. These last two formation methods are not discussed here since it was

found that these formation methods contributed very little to NO_x pollutant concentrations for this combustion system.

Thermal NO_x is very temperature dependent and very prominent at temperatures above 1850K. In this formation method, nitrogen from the air is oxidized to form NO. The formation of NO by this method is summarized by the well known Zeldovich mechanism [15],

$$O + N_2 \rightleftharpoons N + NO \tag{2.41}$$

$$N + O_2 \rightleftharpoons O + NO \tag{2.42}$$

$$N + OH \rightleftharpoons H + NO \tag{2.43}$$

Reaction rates for these equations have been found by experimenters to be [16],

$$k_{f,1} = 1.8(10^8)e^{-38370/T} \qquad k_{r,1} = 3.8(10^7)e^{-425/T}, \tag{2.44}$$

$$k_{f,2} = 1.8(10^4)Te^{-4680/T} \qquad k_{r,2} = 3.81(10^3)Te^{-20820/T}, \tag{2.45}$$

$$k_{f,3} = 7.1(10^7)e^{-450/T} \qquad k_{r,3} = 1.7(10^8)e^{-24560/T}. \tag{2.46}$$

To model the formation of this pollutant, first a transport equation is solved for the mass fraction of NO,

$$\frac{\partial \overline{\rho}\widetilde{Y}_{NO}}{\partial t} + \frac{\partial(\overline{\rho}\widetilde{U}_i\widetilde{Y}_{NO})}{\partial x_i} = \frac{\partial}{\partial x_j}(\overline{\rho}\mathfrak{D}\frac{\partial \widetilde{Y}_{NO}}{\partial x_j}) + Sources. \tag{2.47}$$

This equation is solved at the end of the simulation if the RANS turbulence model is used but must be solved throughout a LES so that statistics for a time averaged mean can be collected. The source term is found from the formation of NO by the

Zeldovich mechanism which can be modeled as [17],

$$Source = M_{NO}\frac{d[NO]}{dt}, \tag{2.48}$$

where,

$$\frac{d[NO]}{dt} = 2k_{f,1}[O][N_2]\frac{\left(1-\frac{k_{r,1}k_{r,2}[NO]^2}{k_{f,1}[N_2]k_{f,2}[O_2]}\right)}{\left(1+\frac{k_{r,1}[NO]}{k_{f,2}[O_2]+k_{f,3}[OH]}\right)}. \tag{2.49}$$

When considering equilibrium for the chemistry mechanism, the concentrations of the O radical are calculated using an assumption that the O radicals are formed in a partial equilibrium situation from the dissociation and recombination of O_2 and O. The concentrations of O and OH radicals significantly impact the predicted amount of NO_x and the detailed chemistry used in the flamelet model leads to values of NO_x that are closer in value to those found in the rig data. In Figure 2.7, it can be seen how parameters used in the NO_x model vary with scalar dissipation rate. Using an arbitrary local concentration of NO in the NO_x model of 1e-6, the source term in the pollutant model can be plotted versus equivalence ratio for a given scalar dissipation rate to observe the behavior of the source term which is shown in Figure 2.8. It is obvious from these figures that NO formation is a competition between temperature, [O], and [OH].

2.2.5 Solver

Some methods used to numerically solve the governing equations in ANSYS FLUENT will now be discussed. Details of ANSYS FLUENT's solvers can be found in its theory manual which describes the models of this CFD code [18]. The Mach number based upon the annulus inlet is much less than 0.3 and local mach numbers remain below 0.30 everywhere expect for a few places such as the mixing jets where the Mach number climbs to around 0.30. This justifies the use of the pressure based

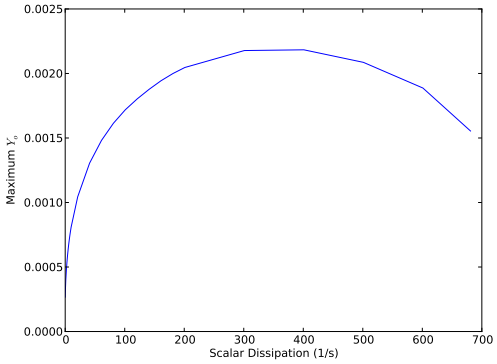

(a) O dependence on χ

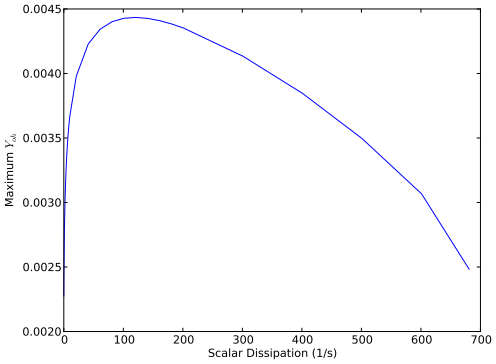

(b) OH dependence on χ

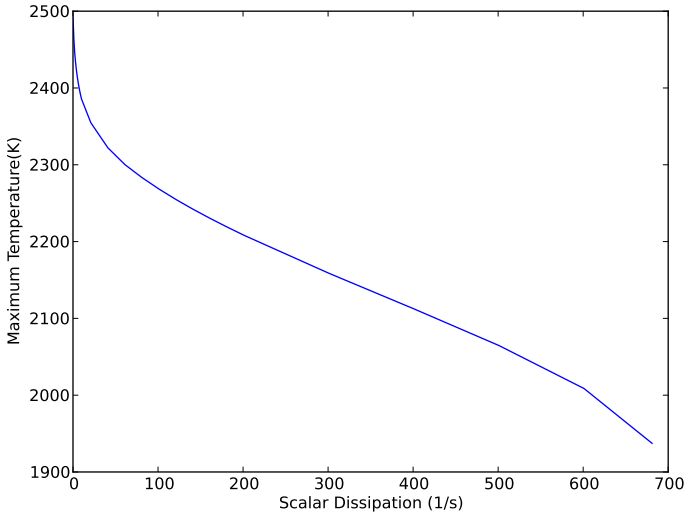

(c) Temperature dependence on χ

Figure 2.7: Flamelet library reactive scalars as a function of scalar dissipation rate.

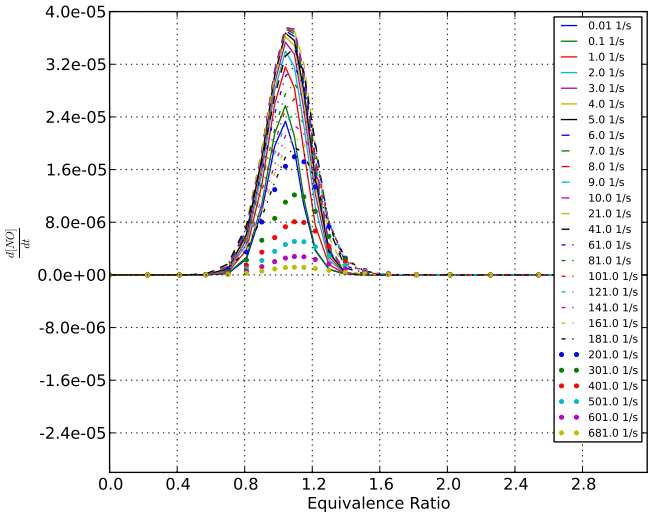

Figure 2.8: Source term used in NO_x model

solver which is suitable for low Mach number flows. When using this solver, a pressure equation is formed using the continuity and momentum equations. A coupled pressure-velocity scheme was used so that the momentum and pressure equation are solved simultaneously. The overall solution process for a steady simulation is summarized by Figure 2.9. Steady simulations were used for the RANS turbulence model whereas transient or unsteady simulations were used with the LES turbulence model. For unsteady simulations the steady loop is solved for a short number of iterations (20 iterations) and then the equations are advanced in time.

2.3 Results

Simulations using the RANS turbulence model were iterated until the solution was converged which was established as when the residuals of each equation solved for was sufficiently small and was no longer significantly changing. A typical set of residuals for a RANS simulation is shown in Figure 2.10. In this figure, the residuals for continuity, momentum, energy, turbulence equations, and combustion equations

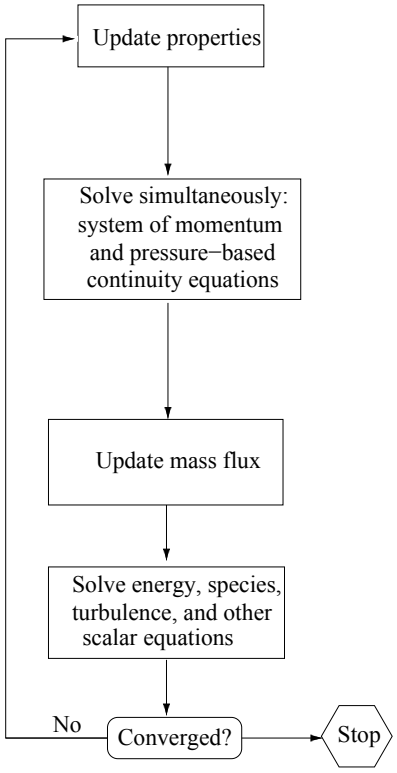

Figure 2.9: Solution iteration loop for steady calculations [18].

are of the order 1e-2, 1e-5, 1e-4, 1e-5 respectively. For the last 500 iterations, the residuals level off and oscillate around those values. Conservation checks of mass and mixture fraction confirm the simulations were converged. Additionally, the average temperature at the exit was recorded and was observed to converge, which can be seen in Figure. Large Eddy Simulations were then performed using the RANS solution as an initial solution. The residence time of a combustor can be defined as,

$$t_{res} = \frac{m}{\dot{m}} = \frac{\rho \forall}{\dot{m}}. \tag{2.50}$$

LES was performed for $10t_{res}$ with the last half of the simulation being used to collect time averaged statistics such as mean and root mean square (RMS) values of

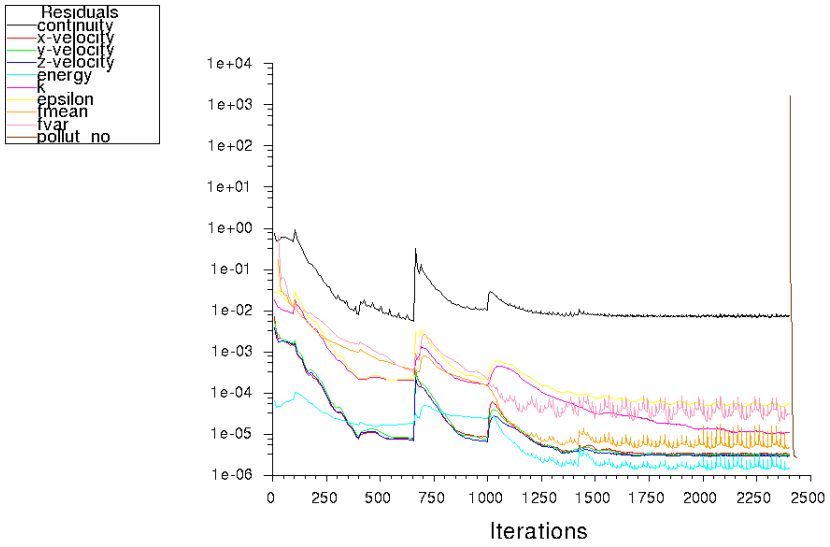

Figure 2.10: Set of residuals for RANS simulations.

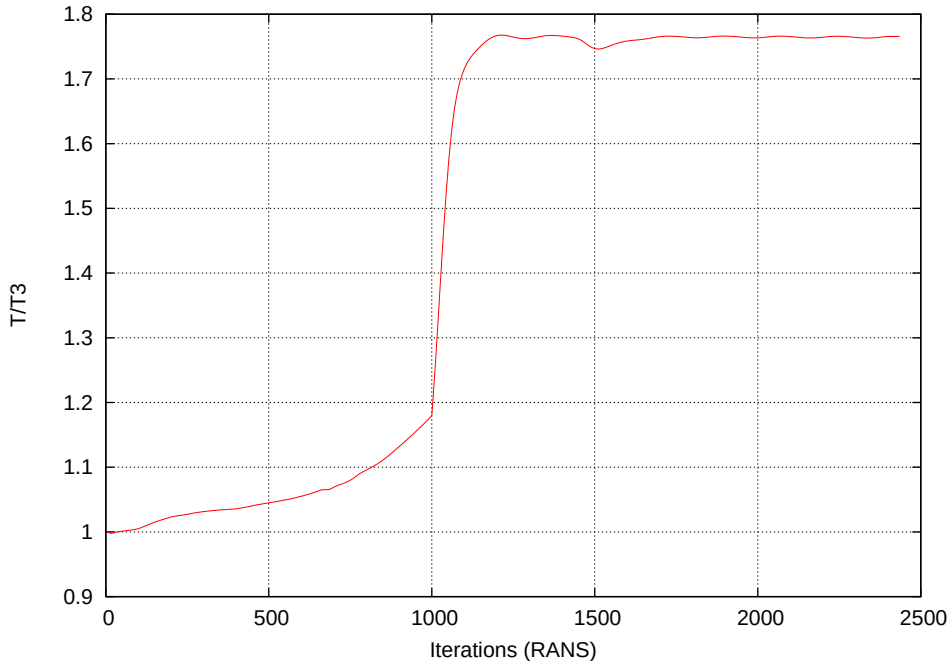

Figure 2.11: Convergence of average exit temperature.

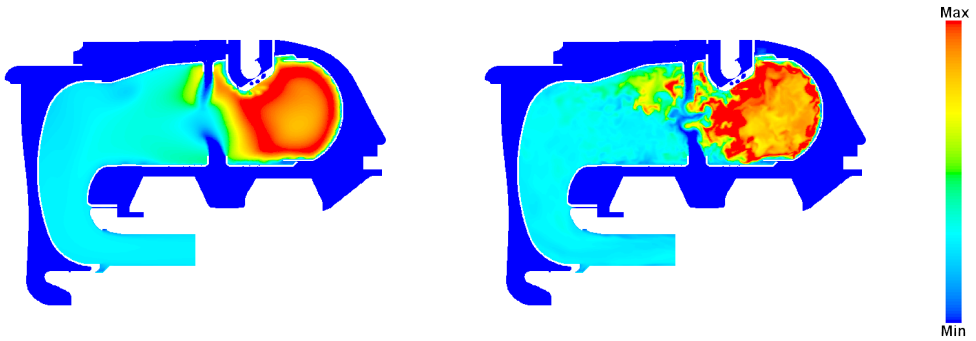

(a) RANS turbulence model. (b) LES turbulence model.

Figure 2.12: Temperature distribution. Mean temperature field is shown for RANS and instantaneous field is shown for LES.

the instantaneous fields that are solved for in an LES. Mean fields were used from the LES to compare with RANS and rig data. For solution visualization purposes, temperature distribution on the center plane of the sector using the RANS and LES turbulence models are shown in Figure 2.12a and Figure 2.12b, respectively.

Computational results from the three configurations (Test 3a, Test 3b, Test 3c, which correspond to the swirlers shown in Figure 2.2), are compared to rig data. Recall that the three configurations differ among each other by the swirler geometry surrounding the atomizer. A few metrics will first be discussed that were used to compare the two sets of results. NO_x pollutants were measured by an emission index (EI) which is defined as,

$$EI_{NO_x} = \frac{1000 Y_{no} \dot{m}_{exit}}{\dot{m}_{fuel}} \doteq \left[\frac{g}{kg\ fuel} \right]. \tag{2.51}$$

The pattern factor (PF) is a metric that shows how uniform the exit temperature is and is important for the life of the turbine. The pattern factor is defined as,

$$PF = \frac{T_{max} - T_{exit\ avg}}{T_{exit\ avg} - T_{inlet}}. \tag{2.52}$$

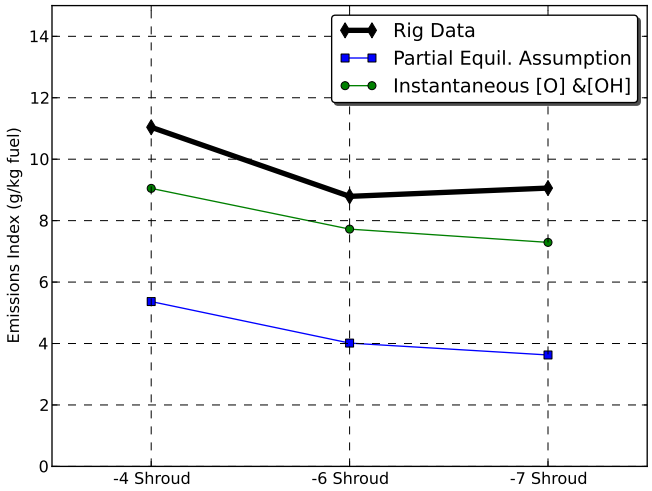

Figure 2.13: Effect of radical concentrations used in the pollutant model.

Figure 2.13 shows pollutant results from a RANS simulation with a flamelet model. One model uses the detailed chemistry of the flamelet model to calculate the source term radicals in the pollutant model while the other uses a partial equilibrium assumption to calculate radicals. The partial equilibrium assumption used in the pollutant model does not take advantage of the detailed chemistry in the flamelet model since it uses $[O_2]$ to calculated $[O]$ radicals from the reaction equation,

$$O_2 + M \leftrightharpoons O + O + M, \tag{2.53}$$

where M is a third body. The results of this figure show the increased accuracy of using the flamelet model's detailed chemistry for NO_x concentration predictions. Note also that the goal is to validate the CFD models across these three configurations so it is important to not only compare quantitative values but also look at whether or not the trend in numerical data among the configurations is consistent with the rig data.

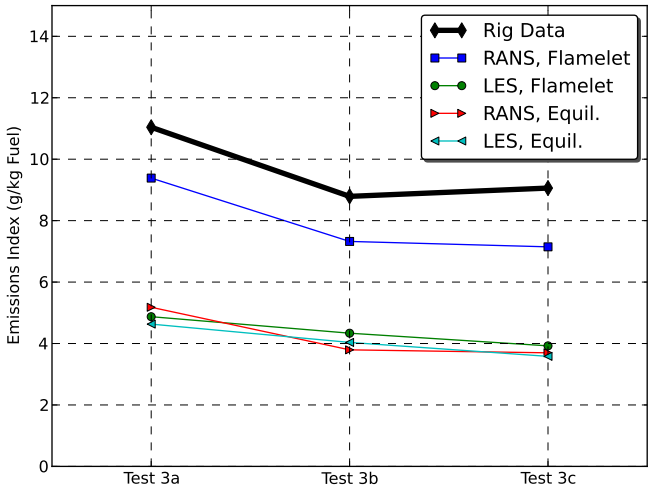

Figure 2.14: NO_x EI for all turbulence and combustion models used.

Figure 2.14 compares pollutant results for all turbulence and combustion/chemistry models used. With the LES turbulence model a decrease in levels of NO_x was seen when using the flamelet model relative to levels seen with RANS and flamelet models. It will be shown in Chapter 4 that the primary zone is more rich in LES and as the equivalence ratio moves away from stoichiometric value, $\phi = 1$, the temperature as well as NO_x decrease. Both turbulence models using the equilibrium model show lower NO_x concentrations due to the partial equilibrium assumption to calculate radical concentrations for the NO_x source term and both models show similar values for each configuration.

Experimental temperature distributions at the exit of the combustor were available from a thermocouple rake. These were compared with temperature contours from the computational results. The temperature distribution in the rig data is very uniform compared to the CFD data. In Figure 2.15 - Figure 2.17 exit temperature distributions are shown on the same non-dimensional scale as the rig data. To see

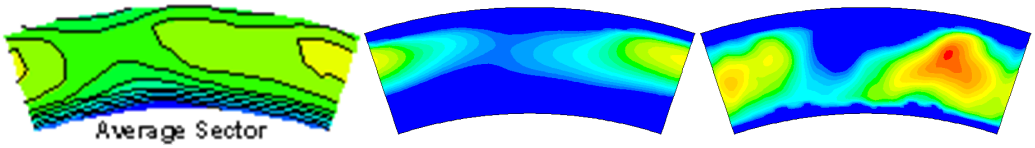

(a) Rig Data (b) RANS Turbulence Model (c) LES Turbulence Model

Figure 2.15: Exit temperature contours of Test 3a with equilibrium model.

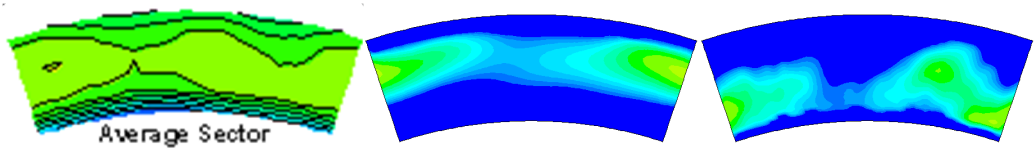

(a) Rig Data (b) RANS Turbulence Model (c) LES Turbulence Model

Figure 2.16: Exit temperature contours of Test 3b with equilibrium model.

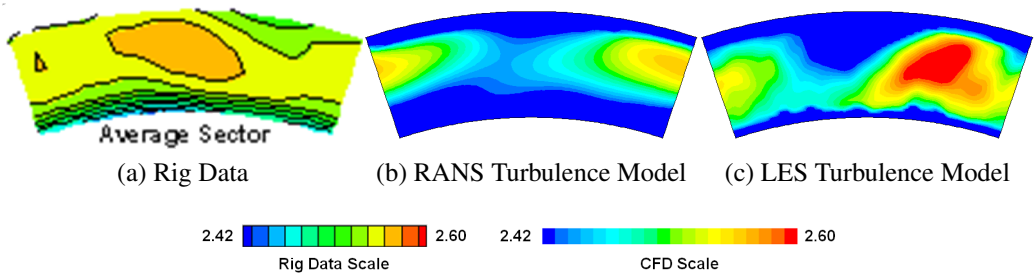

(a) Rig Data (b) RANS Turbulence Model (c) LES Turbulence Model

Figure 2.17: Exit temperature contours of Test 3c with equilibrium model.

more details in the figures the lower limit of the temperature scale is decreased and used in the following figures.

A radial profile at the exit of the combustor was also compared to values from the experimental data which is shown in Figure 2.24 - Figure 2.26 for the three configurations.

Lastly, Figure 2.27 shows pattern factors for the three configurations using all the models.

2.4 Conclusions

Using these results, it is possible to make some initial observations and conclusions. Using RANS with the flamelet model, the NO_x model misses the last trend in data

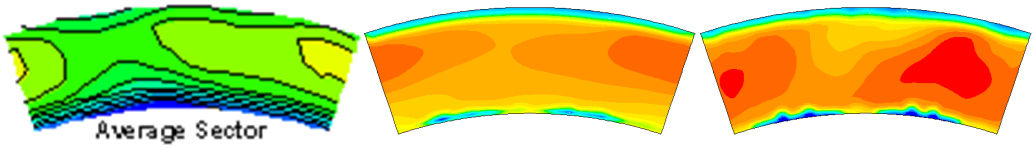

(a) Rig Data (b) RANS Turbulence Model (c) LES Turbulence Model

Figure 2.18: Exit temperature contours of Test 3a with equilibrium model (rescaled).

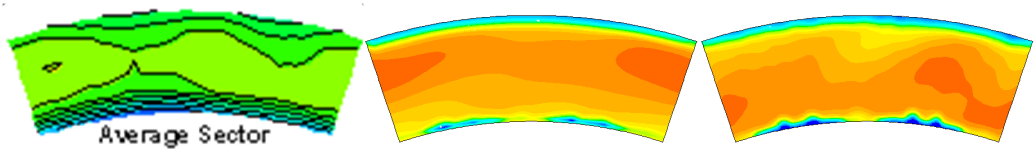

(a) Rig Data (b) RANS Turbulence Model (c) LES Turbulence Model

Figure 2.19: Exit temperature contours of Test 3b with equilibrium model (rescaled).

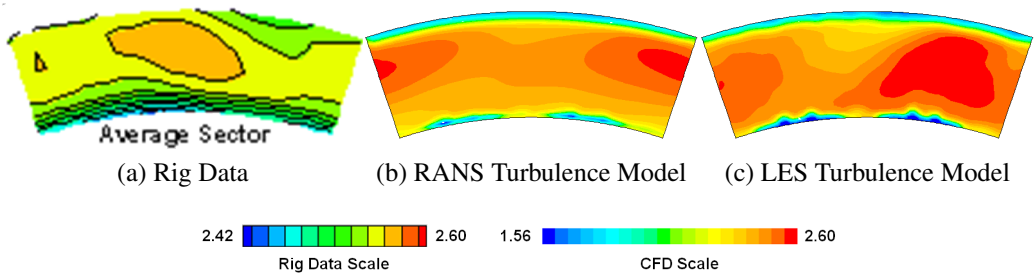

(a) Rig Data (b) RANS Turbulence Model (c) LES Turbulence Model

Figure 2.20: Exit temperature contours of Test 3c with equilibrium model (rescaled).

where it is expected to increase but the CFD shows a decrease. Otherwise, there is an almost constant delta between the rig data and numerical results. Both sets of data using the LES turbulence model show large under predictions as well as showing no consistent trend with the rig data.

Comparing rescaled exit temperature distributions, it is evident that the RANS model for either chemistry model captures the correct pattern of hot spots for the first two configurations. In the third configuration, a hot spot is seen in the center of the sector which is captured better in LES.

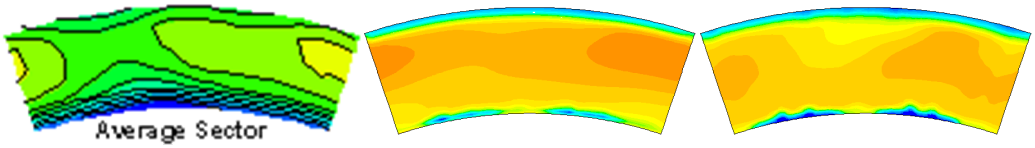

(a) Rig Data (b) RANS Turbulence Model (c) LES Turbulence Model

Figure 2.21: Exit temperature contours of Test 3a with flamelet model.

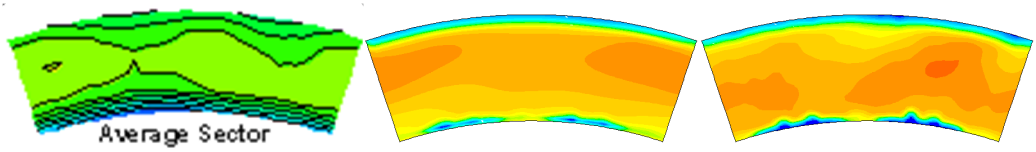

(a) Rig Data (b) RANS Turbulence Model (c) LES Turbulence Model

Figure 2.22: Exit temperature contours of Test 3b with flamelet model.

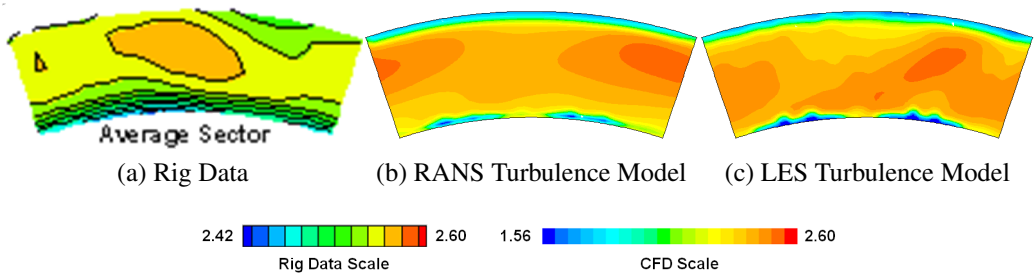

(a) Rig Data (b) RANS Turbulence Model (c) LES Turbulence Model

Figure 2.23: Exit temperature contours of Test 3c with flamelet model.

All radial profiles show colder temperatures at the hub of the exit. The cause and solution to this will be shown later as a factor attributed to mesh resolution. In Test 3a, LES shows a more uniform, flatter profile with the same peak span position as the rig data. In the other two cases, RANS and LES disagree with the position of peak temperature and neither match rig data very well.

Pattern factor appears to be predicted completely wrong with RANS, which has the opposite trend as the rig data. LES results show an improvement, with a correct trend from Test 3a to 3b. However, LES over predicts the PF for all configurations.

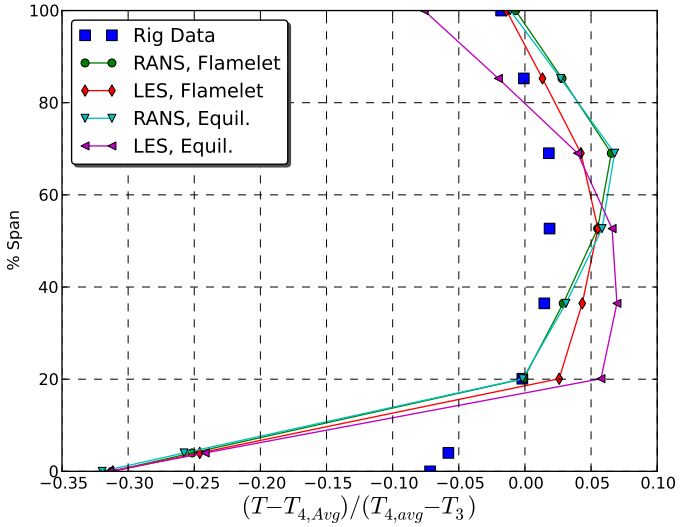

Figure 2.24: Radial temperature profile of Test 3a.

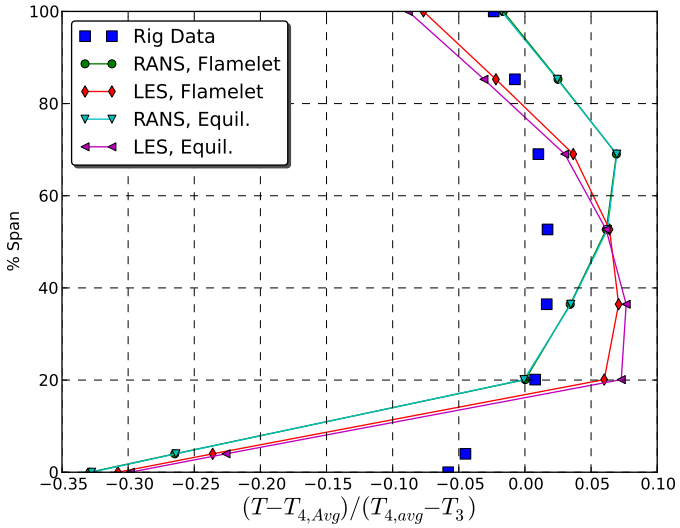

Figure 2.25: Radial temperature profile of Test 3b.

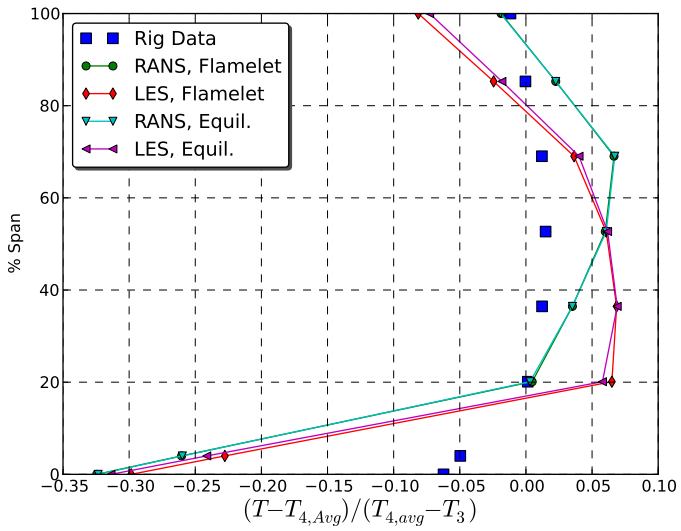

Figure 2.26: Radial temperature profile of Test 3c.

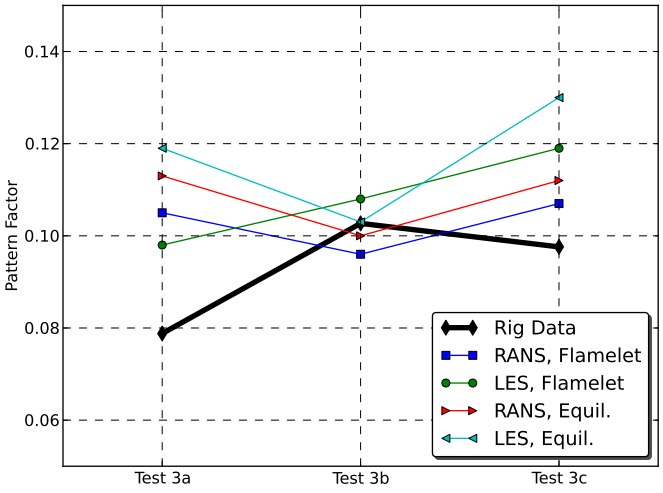

Figure 2.27: Pattern Factor for all turbulence and combustion models used.

Chapter 3

Fuel Spray Modeling

3.1 Background

Next, the atomization model and fuel boundary conditions used for the fuel spray in the combustor simulations were evaluated. Experimental characterization of the dual orifice pressure atomizer used in the combustor had been previously performed and the results of this experiment were used to evaluate numerical simulations.

Pressure swirl atomizers are commonly used in gas turbine combustors. Inlet ports in the atomizer inject fuel tangentially into a chamber causing the fuel to swirl around the sides of the swirl chamber developing an air core in the center. The fuel then exits through an orifice as a sheet in the shape of a hollow cone. The sheet breaks up due to aerodynamic forces and surface tension to form ligaments and eventually droplets. The dual orifice pressure swirl atomizer is basically a single orifice pressure swirl atomizer or simplex atomizer, mounted inside a larger one and is used since this type of atomizer offers better performance across a range of fuel mass flow rates compared to the single orifice pressure swirl atomizer. The atomizer is mounted in a shroud, see Figure 3.1. Such an atomizer-shroud configuration is commonly used in tangentially fuel-injected combustor chambers of APUs on aircrafts. Since modeling the primary atomization of the atomizer is not practical in combustor simulations, atomization models are usually relied upon to supply fuel boundary conditions based on known conditions of the atomizer.

Two atomization models were evaluated and fuel spray boundary conditions were developed to be used in future combustor simulations. The first model evaluated is based on a common practice of implementing fuel boundary conditions and is similar to the boundary conditions used in the baseline simulations. In this method the spray is considered to be already atomized and the range of diameters is

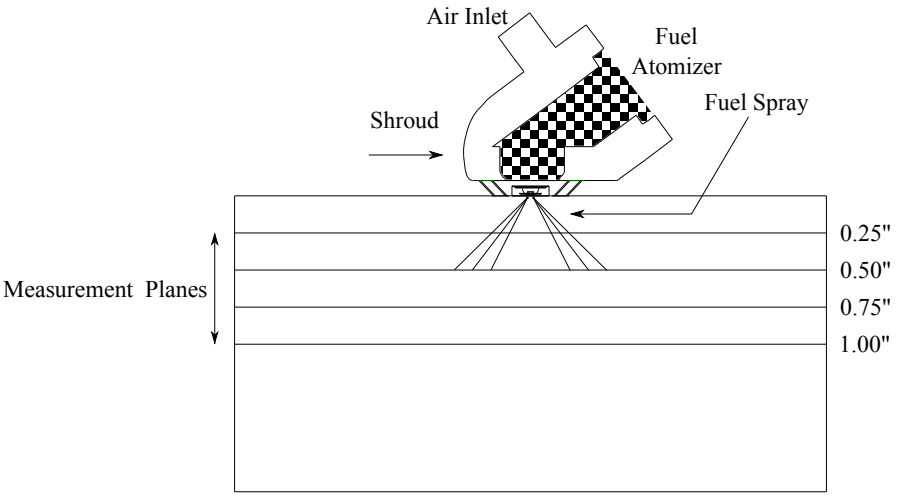

Figure 3.1: A 2D cross section of the simulated pressure chamber geometry showing the shroud configuration mounted above the four measurement planes.

input by a distribution function such as that of Rosin-Rammler. Parameters of this model were adjusted according to a case without shroud air with the aid of experimental data. This model was then used with the three same shroud configurations used in the combustor. No further adjustments were made to the spray model except for the addition of a secondary breakup model to account for breakup caused by the shroud air. Note the difference between the baseline method of inputting a diameter distribution from experiments for all three shrouds and this new method. The second atomization model used is based on the ”blob” injection method [19]. Here large droplets or ”blobs” are injected independent of the size distribution found downstream of the atomizer. In this atomization model, a breakup model is used to represent both primary and secondary atomization.

3.2 Setup

The results of an experimental study previously performed at Honeywell were used to characterize the performance of the pressure atomizer with and without the air shrouds. Fuel sprays exhibit remarkably different behaviors under pressure as op-

posed to ambient pressures. Due to this, the experiments were performed in a pressurized environment to resemble conditions in an actual combustor. Detailed information on the pressure chamber and the measurement system are described by Lai et al. [20]. Fuel nozzles are housed in an air shroud and optical access in the pressure chamber allow laser sheets to pass through the spray. Measurements are taken on four planes perpendicular to the spray axis, see Figure 3.1. Particle Image Velocimetry (PIV) was applied to give spatial distributions of velocity. Planar Light Induced Fluorescence (PLIF) and Planar Laser Mie Scattering were also applied. Taking a ratio of the last two calibrated measurements gives spatial distributions of the Sauter mean diameter. Four cases were analyzed. The first case (Case A) did not have any shroud air present. The other three cases (Case B, Case C, and Case D) used the same atomizer conditions as Case A but used shroud air to increase atomization. The same shrouds shown in Figure 2.2 surround the atomizer and promote further atomization of the spray. The three shrouds correspond to the same shrouds used in the baseline combustor simulations which are summarized in Table 3.1. The operating temperature of both the fuel and the air was 80°F so the rate of evaporation is small but nonetheless is still active in the simulations.

Table 3.1: Swirlers used in spray modeling study.

Case	Swirlers
A	None
B	S3a
C	S3b
D	S3c

A subsection of the environment in which the experimental data was taken, was reproduced and meshed for computer simulations. This subsection is composed of a cylindrical section, the top surface being the location of the shroud and atom-

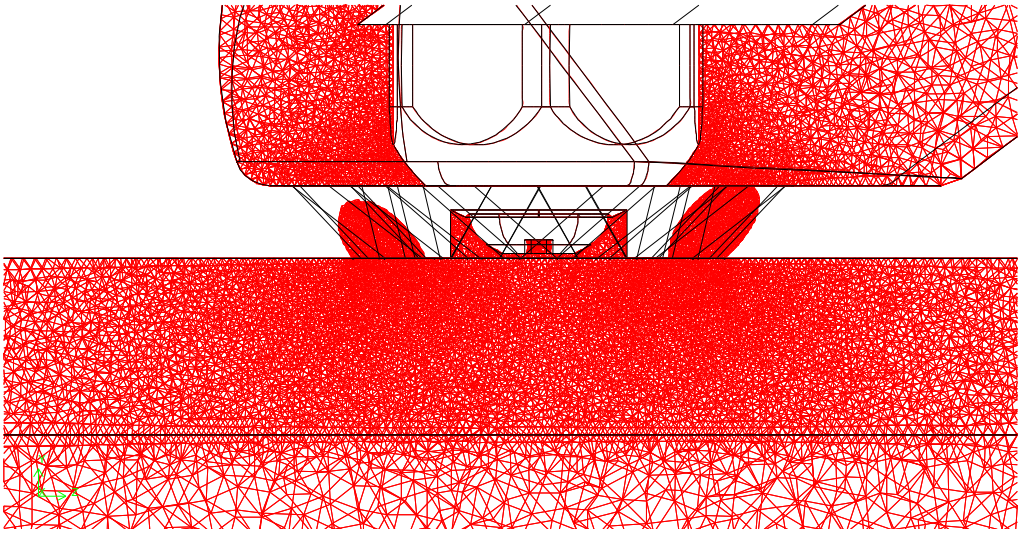

Figure 3.2: 2D cross section showing the mesh of the pressure chamber.

izer, down to a fuel/air extraction. The sides of the cylinder have a radially inward mass flow. A 4 million cell hybrid mesh was generated with refinement near the atomizer's location, see Figure 3.2.

The same physical models from the combustor simulations were used for these cases where applicable. To summarize: RANS and LES turbulence models were used and a coupled Eulerian/Lagranian two way coupled discrete phase model was used. However, one change to the set of models used for these simulations is the addition of a secondary breakup model. Details of secondary breakup models will be discussed in Section 3.3.

3.3 Atomization Models

3.3.1 Primary Atomization Model 1 (PAM1)

Since the complex interactions that initially atomize the fuel are computationally expensive to simulate in combustor simulations, the primary atomization must be represented by a model. As previously mentioned, in this first model the spray is considered to be already atomized at the point of injection. To model the dual

orifice atomizer, two sets of droplet injections were used, one for the primary orifice and the other for the secondary orifice. These droplets were injected in the shape of a cone with a specified mean spray angle and dispersion angle. To estimate a mean spray angle, mass density distributions on a horizontal plane 0.25" from the atomizer location were analyzed for Case A. The radial position of the maximum mass density was found and this was used to assign the mean spray angle. The radial distance between the maximum mass density and the edge of the spray was used to compute a dispersion angle. The velocity of the droplets also needs to be input. Schmidt [21] gives an estimate for the velocity of the fuel as,

$$U = k_v \sqrt{\frac{2\Delta p}{\rho_l}}, \tag{3.1}$$

where:

$$k_v = max\left[0.7, \frac{4\dot{m}}{\pi {d_0}^2 \rho_l cos(\theta)} \sqrt{\frac{\rho_l}{2\Delta p}}\right]. \tag{3.2}$$

Note that Equation (3.1) is the same as Equation (2.3) except now a velocity coefficient is used. The reasoning for this is some kinetic energy of the drops is lost in primary atomization. The constant $k_v = 0.7$ is found to produce velocities larger than those found in experimental results; however, this constant is dependent on the atomizer. The velocity coefficient was determined by assessing velocity distributions on the three downstream planes for different values of k_v. $k_v \approx 0.5$ produced velocity distributions that matched experimental data reasonably well on the three downstream planes. Similar to the baseline simulations, a SMD and Rosin-Rammler spread were used to input a diameter distribution but in these simulations only the diameter distribution for the case with no shroud air is used. After the model properly reproduced the performance of Case A, this model was used for the other three shroud air cases with the addition of a secondary breakup model.

The WAVE breakup model and a stochastic secondary breakup model were used. The breakup model used by Reitz [19] in the plain orifice pressure atomizer is the WAVE breakup model. The WAVE breakup model is formed by first numerically solving a dispersion relationship which is the result of a stability analysis of the liquid surface of a cylindrical jet subject to perturbations. Curve fits of the numerical solutions yield expressions for the fastest growing wave and maximum wave growth rate. In this breakup model the radius of the droplets shed from the blobs is proportional to the wavelength of the most unstable wave on the surface of the blob:

$$r = B_0 \Lambda \tag{3.3}$$

The proportionality factor, B_0, can be used as a tuning constant for the model. A value of 0.61 is given by Reitz. Obviously, lowering this constant will decrease the size of the "child" droplets shed.

The rate of change in the blob radius, a, is given by:

$$\frac{da}{dt} = -(a - r)/\tau \tag{3.4}$$

where:

$$\tau = \frac{3.726 B_1 a}{\Lambda \Omega} \tag{3.5}$$

The expression for the breakup time also has a proportionality factor, B_1, that ranges between 1 and 60 and is dependent on the injector characterization. A value of 1.73 is recommended by O'Rourke [22]. A study involving changing these model parameters was conducted but based upon the results the recommended value provided the best results for the cases considered and therefore, the recommended values for con-

stants B_0 and B_1 were used with the PAM1 (and also PAM2) in the WAVE breakup model.

In addition to the WAVE breakup model, simulations using a stochastic secondary breakup model were also performed. The stochastic breakup model is reviewed by Apte et al. [23]. This breakup model has been shown to be capable of accurately describing the breakup of droplets from complex fuel injectors [24]. In this model, breakup is viewed as a discrete random process and governed by the Fokker-Plank differential equation. The Lagranian tracking scheme differs from that of the WAVE model. In the WAVE breakup model, as a parent droplet breaks up, new parcels are created. However, as breakup occurs in the stochastic model, the diameters of the droplets decrease and the number of droplets increase to conserve mass but the droplets remain in the same parcel until a droplet per parcel threshold is reached. Decreasing the number of target particles (i.e. droplets) per parcel, which increases the number of tracked parcels, increases the expense of the simulation. In PAM1, a large number of parcels are injected at the beginning of each time step and the secondary breakup model is not sensitive to the particles per parcel threshold.

3.3.2 Primary Atomization Model 2 (PAM2)

The second atomization model used was the blob injection model. The blob injection model initially used in plain orifice pressure atomizers, attempts to include a core of unbroken liquid which can be seen in experiments [19]. Using the same principle, the blob model is used here to include some effect of the intact hollow cone sheet and model primary atomization. This model relies on the secondary breakup model to correctly predict drop size distributions for all four cases. The same breakup models previously described are used with this model as well. Similarly to PAM1, the blobs are injected in the shape of a cone with one set of injections

representing each orifice. Again a mean spray angle was determined based on mass density distributions on a plane 0.25" from the atomizer. The velocity of the blobs was increased compared to PAM1 since the blobs would not breakup sufficiently at lower velocities. The velocity coefficient used in Equation (3.1) was set to 1 to maximize breakup. When the blob model is used in plain orifice atomizers the blob diameters are set to the size of the orifice. In the situation of the dual orifice pressure atomizer the reference for the blob diameter is not as clear. In one test case a blob diameter set to the theoretical sheet thickness of each orifice was used and in another test case a blob diameter of $400\mu m$ was used, which is approximately 5 times the sheet thickness of the primary orifice. The model is found to be reasonably insensitive to the initial blob size at the velocities encountered in the pressure atomizer. The parameters of the breakup models were also adjusted for this atomization model in Case A only. For the WAVE model, the recommended values were found to yield the best results. The results using the stochastic breakup model were sensitive to the number of particles per parcel. The most accurate results came from lowering this value to around 100 droplets per parcel.

3.4 Results

3.4.1 Atomizer Alone

The four horizontal measurement planes used for the experimental results were recreated in the simulations. Fuel droplet's physical properties were sampled in the simulations as they crossed the four planes. For RANS simulations, droplets were sampled at the end of the simulation. In LES, again the simulation was run for $10t_{res}$ where the residence time is now that of the pressure chamber. A steady spray had developed halfway through the simulation and droplet properties were then collected for the last half of the simulation. The droplet's physical properties were processed to compare to experimental data. Local number averaged axial ve-

locity and local SMD distributions were computed using data from the simulations. Again, it should be noted that PAM1 does not rely on a breakup model for Case A.

Figure 3.3 - 3.9 compare velocity and SMD distributions at the 1.00" downstream plane for Case A using the two primary atomization models with RANS and LES turbulence models. Comparisons show that PAM1 (Figure 3.4 & 3.7) does reasonably well predicting the atomizer's performance. The velocity near the center of the plane is seen to be higher in the simulations. The vortices generated inside the spray cone were found to have an effect on this center velocity and the explanation of the high center velocity in the simulations may be due to weaker vortices in the simulations. Comparisons of SMD distributions show good agreement at the 1.00" plane. The LES results have slightly higher velocities near the center and edges for PAM1.

Results using PAM2 with the WAVE breakup model are shown in Figure 3.5 & 3.8. In Figure 3.6 & 3.9 are results for PAM2 with the stochastic breakup model. PAM2 was not effective in predicting the overall velocity distribution correctly using either breakup model. The larger droplets at the edge of the spray have substantially higher velocity than the experimental data. This suggests that the blob model may not be appropriate for modeling the intact liquid core of the pressure atomizer and its breakup. The atomizer produces large droplets that are traveling slower than those produced in the simulations and the model faces the problem of requiring a high velocity for effective breakup which gives a large velocity to the larger child droplets shed from the blobs. Parameters of the breakup model can be adjusted to try to lower these velocities however the results closest to experimental data came from using the values for the breakup parameters already mentioned. Comparisons of SMD distributions show satisfactory results for PAM2 with the WAVE breakup model. Results using PAM2 with the stochastic breakup model shows a lot of small

droplets remain on the outside of the spray, resulting in lower local SMDs than what are seen in the experimental data. This is due to weak and/or lack of entrainment vortices in the center of the spray which pull the smaller droplets radially inward. Figure 3.10 compares vectors of velocity magnitude for the two atomization models. PAM1 shows the vortical structure in the center of the spray which is responsible for entraining the smaller droplets. Gas velocities from PAM2 show a lack of center vortices. Finally, observe that when using the LES model, more data is present toward the center. Therefore LES results show a slightly greater dispersion with more particles being entrained toward the center which is consistent with data seen from the experiments.

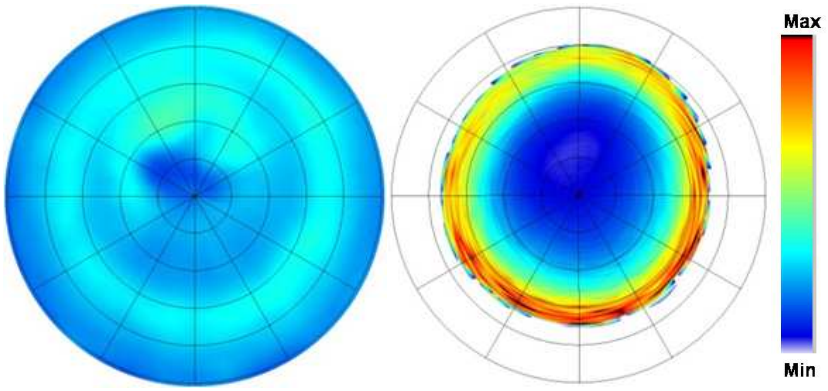

(a) Axial velocity distribution (b) SMD distribution

Figure 3.3: Experimental results for Case A at the 1.00” downstream plane.

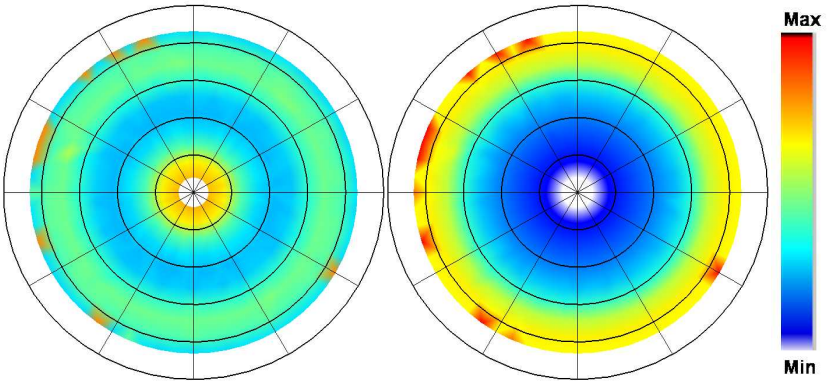

(a) Axial velocity distribution (b) SMD distribution

Figure 3.4: PAM1 results for Case A using RANS at the 1.00” downstream plane. Same scale as in Figure 3.3.

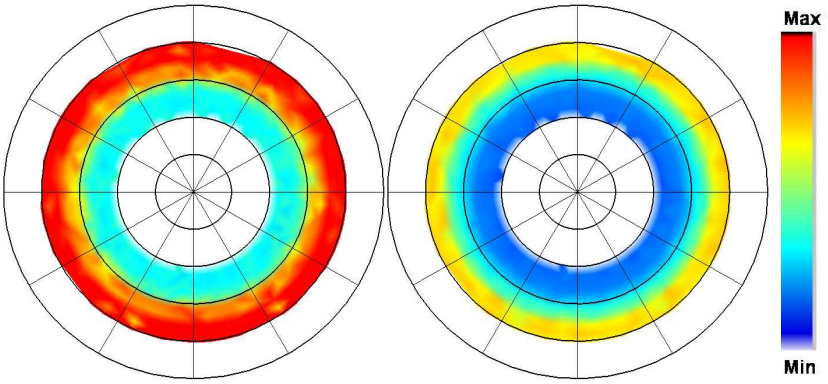

(a) Axial velocity distribution (b) SMD distribution

Figure 3.5: PAM2 results for Case A using RANS and the WAVE breakup model at the 1.00” downstream plane. Same scale as in Figure 3.3.

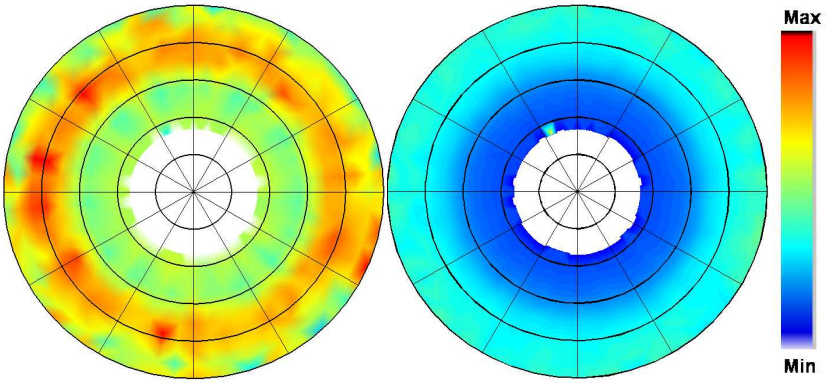

(a) Axial velocity distribution (b) SMD distribution

Figure 3.6: PAM2 results for Case A using RANS and the stochastic breakup model at the 1.00” downstream plane. Same scale as in Figure 3.3.

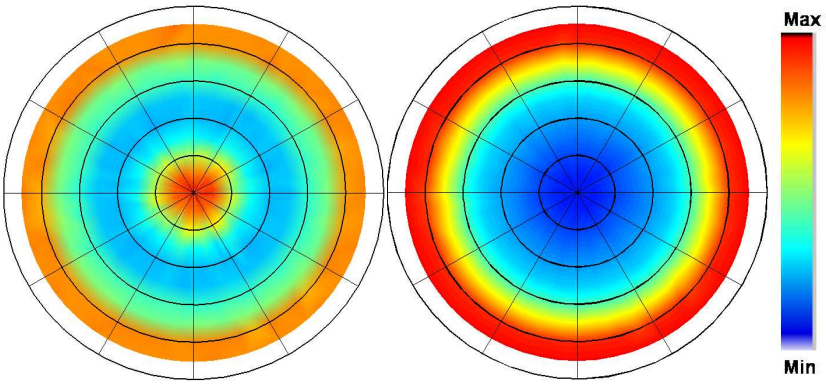

(a) Axial velocity distribution (b) SMD distribution

Figure 3.7: PAM1 results for Case A using LES at the 1.00” downstream plane. Same scale as in Figure 3.3.

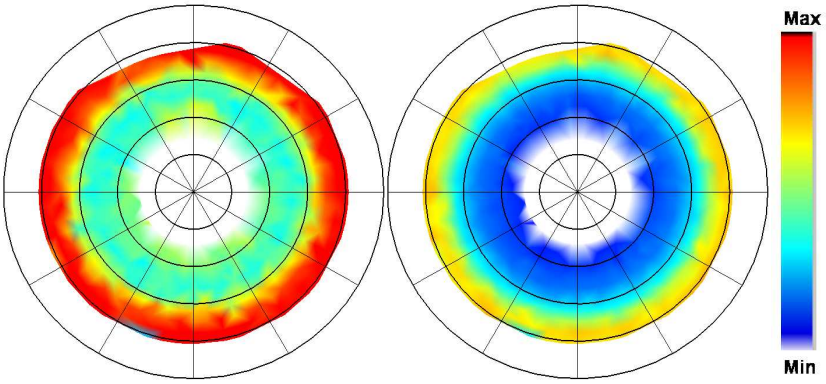

(a) Axial velocity distribution (b) SMD distribution

Figure 3.8: PAM2 results for Case A using LES and the WAVE breakup model at the 1.00” downstream plane. Same scale as in Figure 3.3.

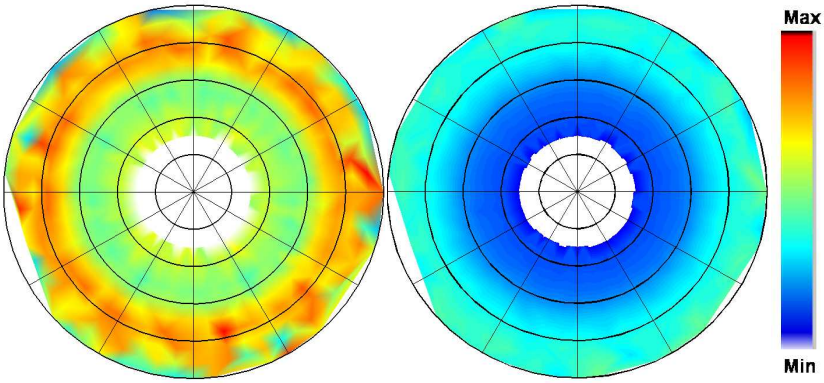

Figure 3.9: PAM2 results using LES and the stochastic breakup model at the 1.00" downstream plane. Same scale as in Figure 3.3.

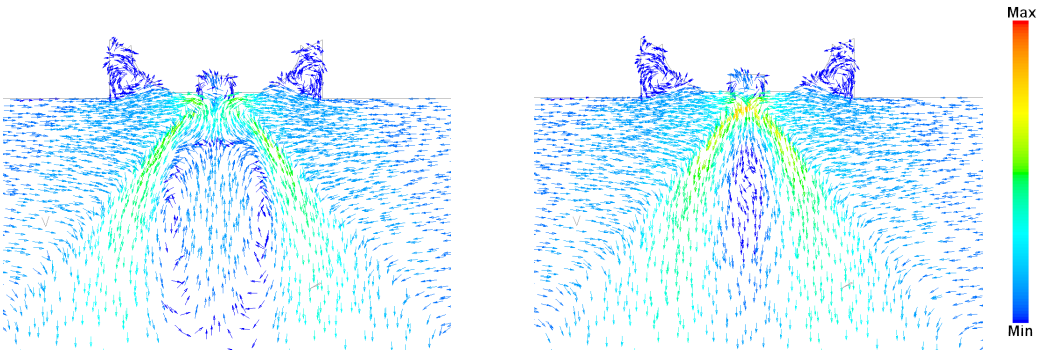

(a) PAM1 (b) PAM2

Figure 3.10: Gas velocity magnitude vectors shown on same color scales.

3.4.2 Atomizer with Shroud

The optimal values for parameters described in Section 3.3 for both models were determined by Case A. These models were then used for the simulations of an atomizer in the presence of shroud air. PAM1 was used with a breakup model to account for the extra atomization produced by the shroud air. PAM2 remains unchanged from Case A. PAM1 and PAM2 were both used with the WAVE breakup model and stochastic breakup model. Initially a RANS turbulence model was used. Figure 3.11 - 3.15 compare velocity and SMD distributions of experimental and

numerical data at the 1.00" downstream plane for Case B. With the presence of shroud air, the velocity of the fuel droplets increases and is close in value to velocities seen in experimental data for all models since the droplets' velocities are primarily determined by the shroud air. All models show a peak velocity region in the top right quadrant but otherwise the overall velocity distribution is not well captured in RANS. SMD distributions are not well captured but do show some similar trends with the center being populated mainly by smaller droplets and larger droplets found at the outer edges of the spray. Experimental data for Case C is shown in Figure 3.16 with data from the simulations shown in Figure 3.17 - 3.20. Experimental data for Case D is shown in Figure 3.21 with data from the simulations shown in Figure 3.22 - 3.25. These two other cases follow similar conclusions of the performance of the models as Case B.

LES of Case B, C, and D are shown in Figure 3.26 - 3.28. PAM1 with the stochastic breakup model was selected for LES of Case B, C, and D. This model was selected based upon previous qualitative results in RANS and a similar trend in the overall SMD at the 1.00" downstream plane shown in Figure 3.29. Overall, LES is shown to predict the atomizer's performance more accurately than RANS. Comparing velocities, the spatial distributions are very similar to the experimental results. Similar patterns are seen and velocities are close to the experimental values. The SMD distribution for Case B show some disparities compared to experimental data. Comparing data for Case C, the same periodic spots of high SMD can be seen at roughly the same radius. In the SMD distribution for Case D, most of the data in the outer edges are low droplet numbers. If this part of the spray is ignored, the SMD distribution is similar to that of the experimental results. Although the distribution is not accurate in Case B, the overall SMD turns out to be comparable to the experimental value. One would expect the overall SMD in Case D to be over

predicted based on Figure 3.28b, however the outer edge of the spray is made of low drop number data from random droplets that manage to escape the shroud air therefore the data at the edge are made of low droplet numbers and the droplets toward the center primarily determine the overall SMD.

Figure 3.29 shows an overall SMD at the 1.00" downstream plane for the four cases. Since the overall SMD is an input for PAM1, the overall SMD for Case A using PAM1 matches the experimental data exactly. PAM1 with the WAVE breakup model under predicts the overall SMD for the three shroud cases. One explanation and improvement for this model might be due to the fact that droplet coalescence was not active during any of these simulations. PAM1 with the stochastic breakup model matches the experimental data nicely for both RANS and LES turbulence models. For all three shroud cases LES yielded a smaller overall SMD than RANS. Based solely on the overall SMD, it is difficult to tell which turbulence model matches the experimental data better but when the distributions of velocity and SMD are taken into account, clearly the LES results are more accurate. PAM2 with the WAVE breakup model largely over predicts the overall SMD for all cases. PAM2 with the stochastic breakup model yielded a close SMD for Case B but over predicted the overall SMD for the other cases.

3.4.3 Conclusions

In the case that the atomizer is modeled without the addition of shroud air, results from PAM1 agree well with experimental data whereas PAM2 over predicts the velocities for the larger droplets. In the cases using additional shroud air, velocities using all models are within range due to the fact that the shroud air increases droplet velocities significantly and primarily determines the range of velocities. PAM1 with a stochastic breakup model produced results that were most similar to the experimental results. Results from LES were shown to improve upon those from RANS

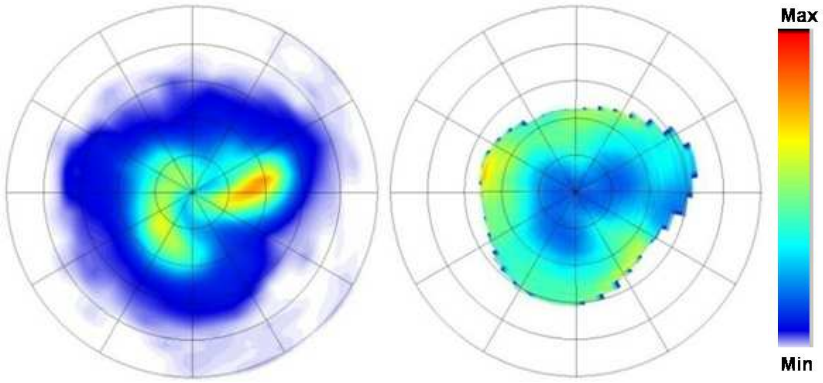

(a) Axial velocity distribution (b) SMD distribution

Figure 3.11: Experimental results for Case B at the 1.00” downstream plane.

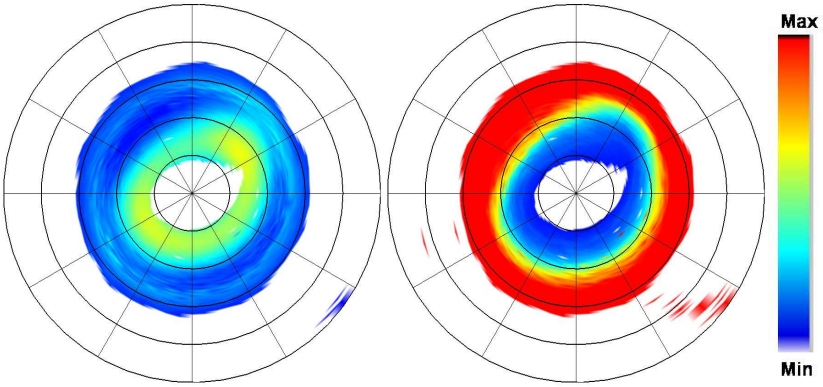

(a) Axial velocity distribution (b) SMD distribution

Figure 3.12: PAM1 results for Case B using RANS with the WAVE breakup model at the 1.00” downstream plane. Same scale as in Figure 3.11.

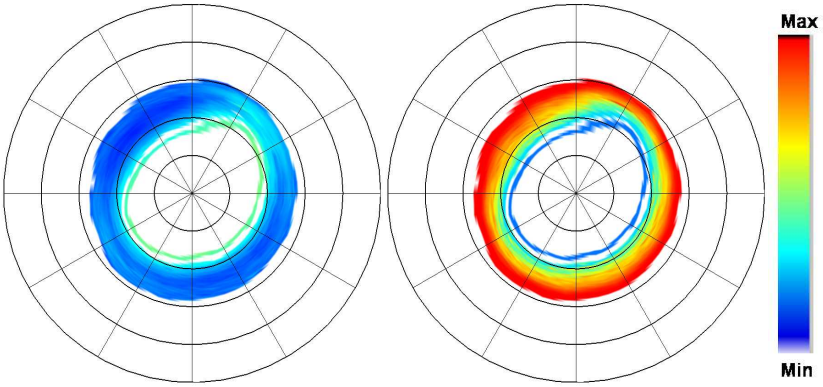

(a) Axial velocity distribution (b) SMD distribution

Figure 3.13: PAM1 results for Case B using RANS with the stochastic breakup model at the 1.00” downstream plane. Same scale as in Figure 3.11.

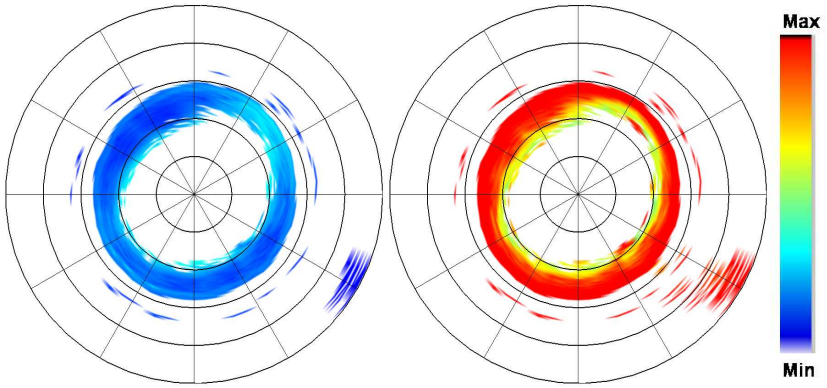

(a) Axial velocity distribution (b) SMD distribution

Figure 3.14: PAM2 results for Case B using RANS with the WAVE breakup model at the 1.00" downstream plane. Same scale as in Figure 3.11.

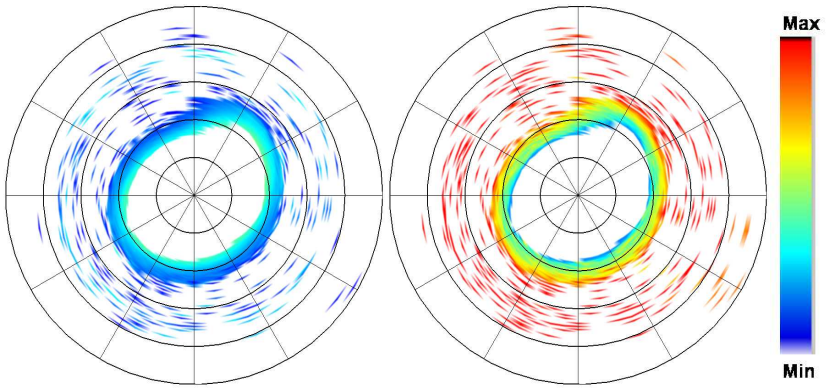

(a) Axial velocity distribution (b) SMD distribution

Figure 3.15: PAM2 results for Case B using RANS with the stochastic breakup model at the 1.00" downstream plane. Same scale as in Figure 3.11.

and were found to give decent spatial descriptions of axial velocity of the droplets as well as local SMDs. Using the results from these simulations, an accurate model for the fuel spray of this dual orifice pressure atomizer can be used for fuel boundary conditions for simulations of the combustor. The model only requires parameters from the atomizer's operating conditions. From the results of these three shrouds it is expected that the model can be used in different combustor and shroud configurations without any experimental fuel spray data that is specific to that configuration.

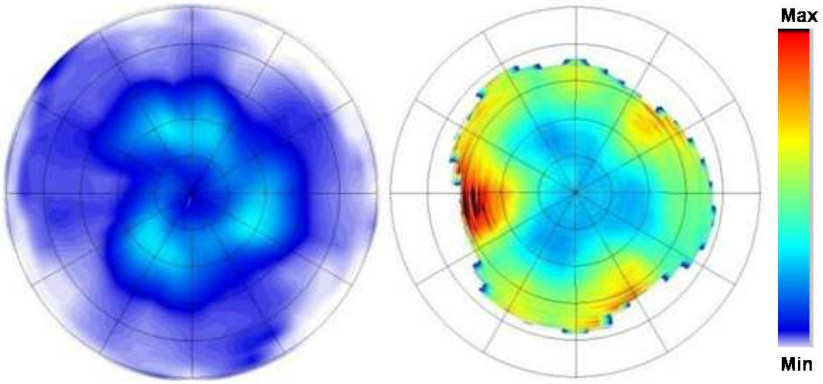

(a) Axial velocity distribution (b) SMD distribution

Figure 3.16: Experimental results for Case C at the 1.00” downstream plane.

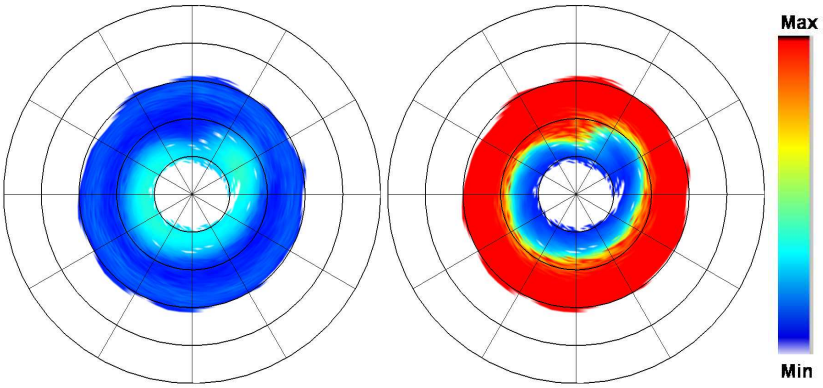

(a) Axial velocity distribution (b) SMD distribution

Figure 3.17: PAM1 results using RANS with the WAVE breakup model at the 1.00” downstream plane. Same scale as in Figure 3.16.

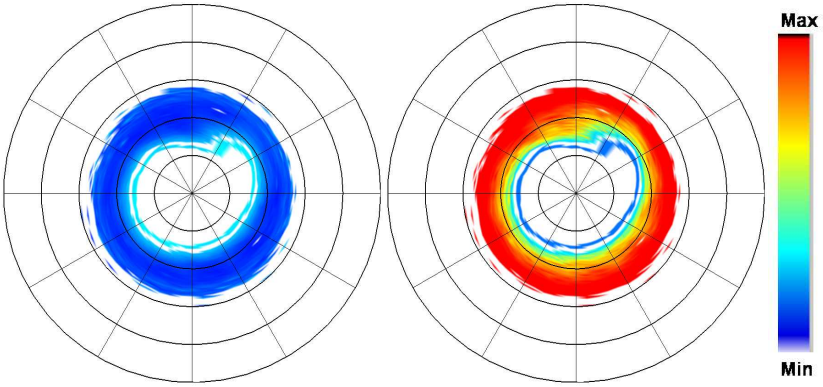

(a) Axial velocity distribution (b) SMD distribution

Figure 3.18: PAM1 results using RANS with the stochastic breakup model at the 1.00” downstream plane. Same scale as in Figure 3.16.

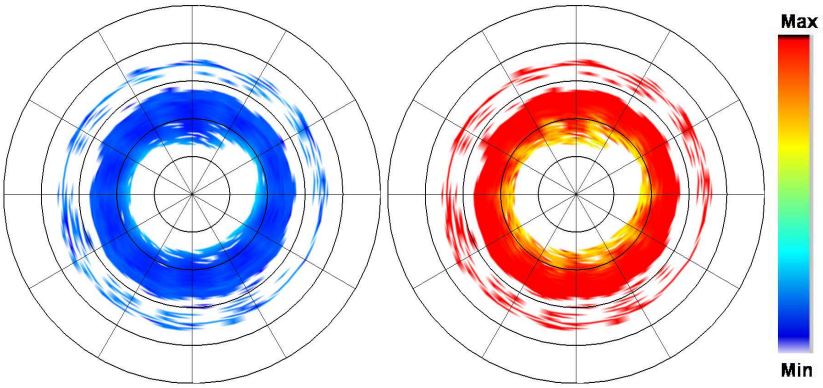

(a) Axial velocity distribution (b) SMD distribution

Figure 3.19: PAM2 results using RANS with the WAVE breakup model at the 1.00" downstream plane. Same scale as in Figure 3.16.

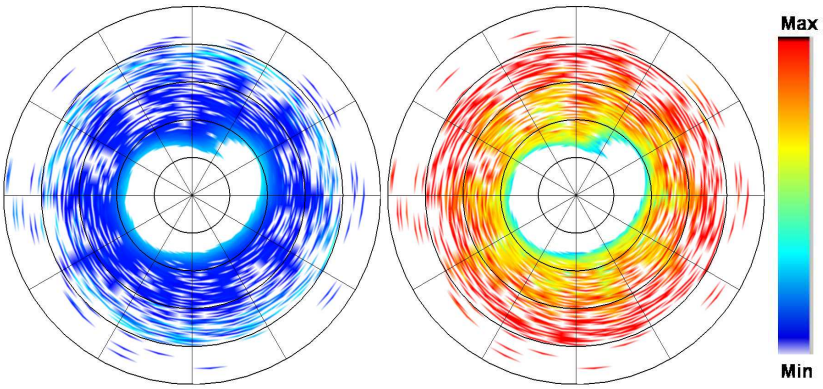

(a) Axial velocity distribution (b) SMD distribution

Figure 3.20: PAM2 results using RANS with the stochastic breakup model at the 1.00" downstream plane. Same scale as in Figure 3.16.

It should be noted however that if the atomizer's operating conditions change, a recalibration process of Case A should be run to re-tune the atomization model parameters.

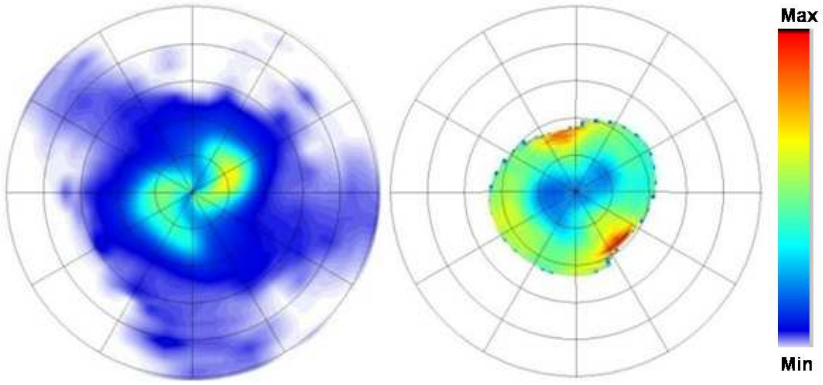

(a) Axial velocity distribution (b) SMD distribution

Figure 3.21: Experimental results for Case D at the 1.00” downstream plane.

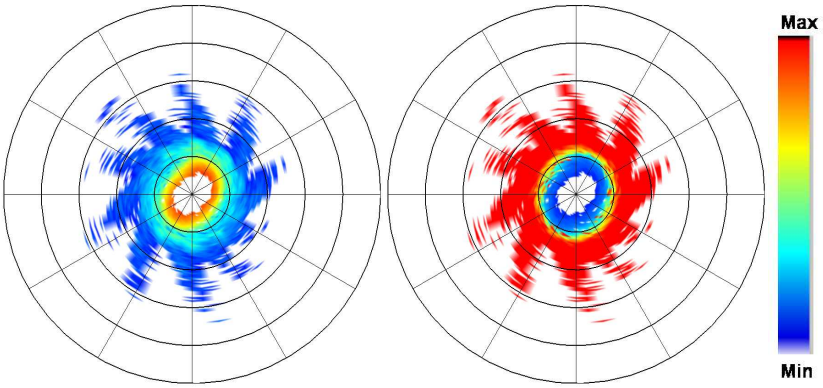

(a) Axial velocity distribution (b) SMD distribution

Figure 3.22: PAM1 results using RANS with the WAVE breakup model at the 1.00” downstream plane. Same scale as in Figure 3.21.

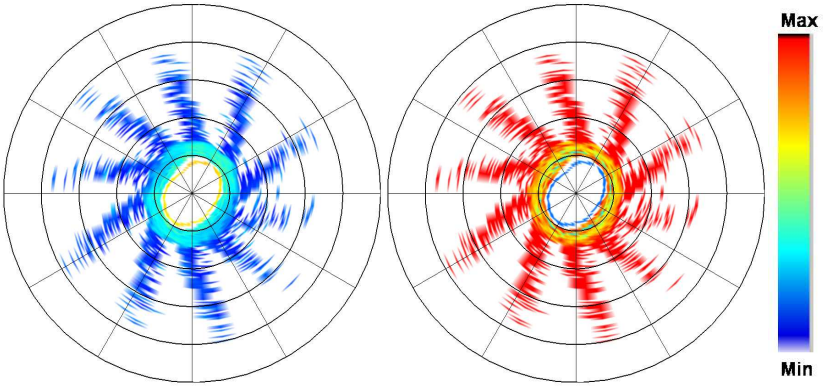

(a) Axial velocity distribution (b) SMD distribution

Figure 3.23: PAM1 results using RANS with the stochastic breakup model at the 1.00” downstream plane. Same scale as in Figure 3.21.

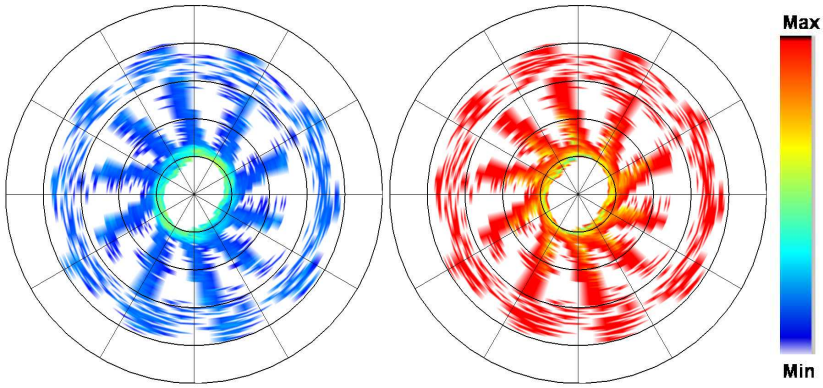

(a) Axial velocity distribution (b) SMD distribution

Figure 3.24: PAM2 results using RANS with the WAVE breakup model at the 1.00” downstream plane. Same scale as in Figure 3.21.

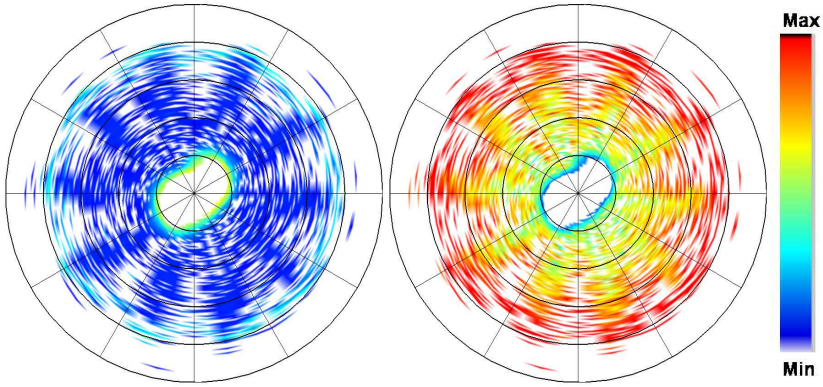

(a) Axial velocity distribution (b) SMD distribution

Figure 3.25: PAM2 results using RANS with the stochastic breakup model at the 1.00” downstream plane. Same scale as in Figure 3.21.

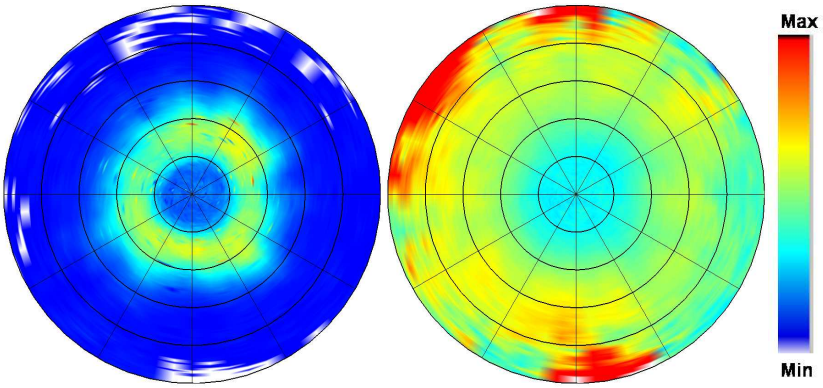

(a) Axial velocity distribution (b) SMD distribution

Figure 3.26: PAM1 results for Case B using LES with the stochastic breakup model at the 1.00” downstream plane. Same scale as in Figure 3.11.

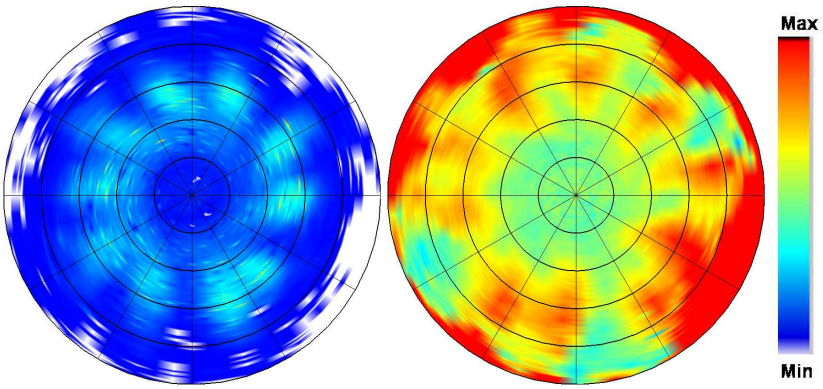

(a) Axial velocity distribution (b) SMD distribution

Figure 3.27: PAM1 results for Case C using LES with the stochastic breakup model at the 1.00” downstream plane. Same scale as in Figure 3.16.

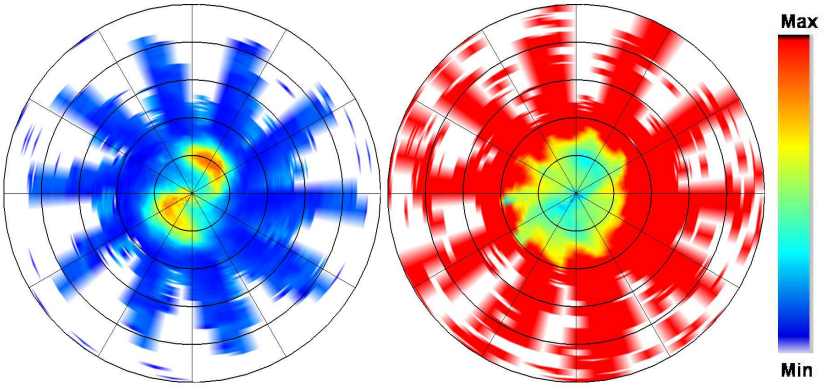

(a) Axial velocity distribution (b) SMD distribution

Figure 3.28: PAM1 results for Case D using LES with the stochastic breakup model at the 1.00” downstream plane. Same scale as in Figure 3.21.

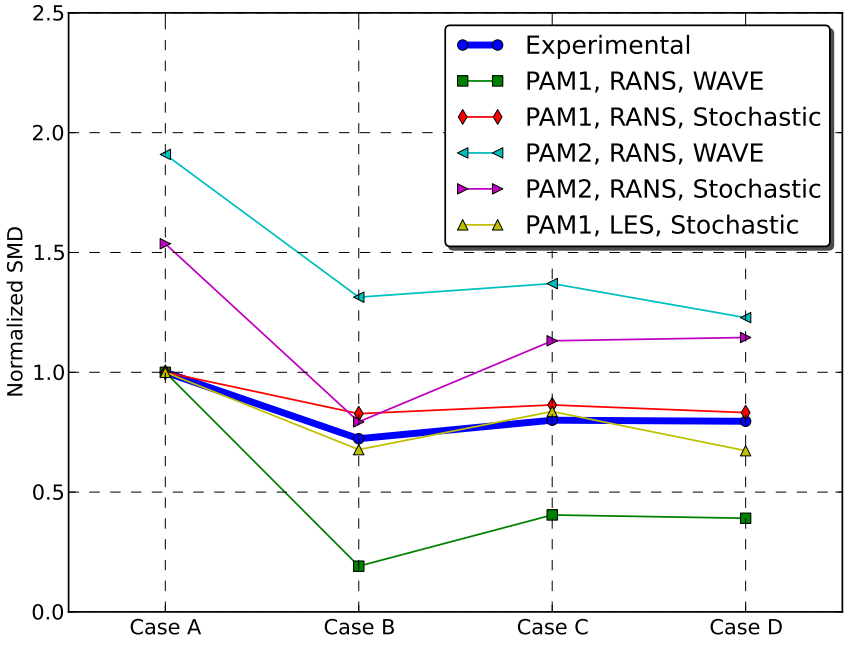

Figure 3.29: Overall SMD at y = 1.00”

Chapter 4

Combustor Modeling Improvements

4.1 Introduction

The same process used to obtain the baseline combustor simulations (see Chapter 2) was run once again with the atomizer model and boundary conditions determined best through the spray modeling study. Once again to clarify the naming convention, the combustor configurations Test 3a, Test 3b, and Test 3c correspond to Case B, Case C, and Case D in the spray modeling study. The difference between the baseline simulations and the following simulations is the spray model. The baseline combustor simulations used a diameter distribution obtained from experimental data and the simulations shown in this chapter use the new spray model. From the spray modeling study, it was shown that the LES turbulence model gives superior results than that of the RANS turbulence model and therefore LES is expected to show greater improvements than that of the RANS simulations.

4.2 Results

In the following figures the baseline data from Chapter 2 is shown along with the combustor simulations using the new spray model. It can be seen in Figure 4.1 that using the equilibrium chemistry model with either turbulence or atomization model leads to significant under prediction of concentrations of NO_x . Additionally, none of these sets of models was able to hold the same trend in NO_x that is seen in the rig data, leading to the conclusion that for NO_x predictions, the equilibrium model is inaccurate.

When the new fuel boundary conditions with the flamelet model is considered in RANS simulations, values slightly closer to rig data values are seen, although the exact trend of the rig data is still not held. With the LES turbulence model, values of NO_x are slightly higher than the previous set of fuel boundary conditions but

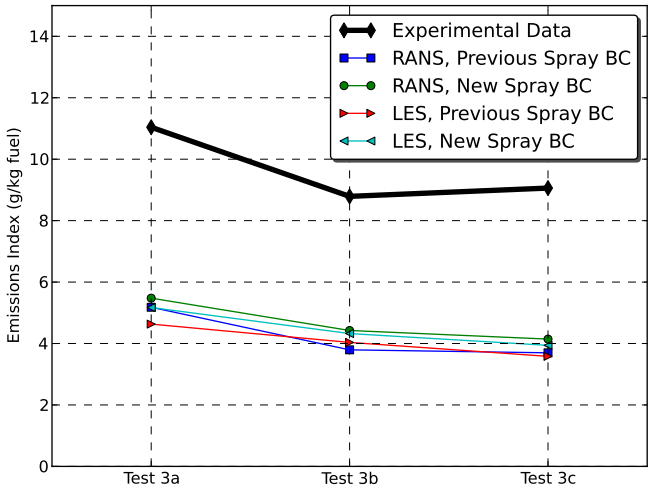

Figure 4.1: NO_x EI for both sets of fuel BC using the equilibrium model.

still are significantly under predicted. However, the trend in NO_x is consistent with rig data. The under prediction of NO_x concentrations in LES seen throughout this work was looked into and is thought to be linked to colder temperatures found in the primary zone of the combustor which can be seen in Figure 4.3. This figure shows average values of temperature on the cross section perpendicular to the axis of the combustor. The data starts at cross sections near the dome of the combustor. Only data from the combustor region is averaged, not data from the annulus. Looking at the mixture fraction in the primary zone, one can see in Figure 4.4 that the RANS simulations have a primary zone that is closer to the stoichiometric value of $Z_{st} \approx 0.0675$ which is why larger concentrations in NO_x are seen.

Pattern factors are shown in Figure 4.5 and Figure 4.6. With the RANS turbulence model, results using the new spray model show PF shifted downward but the trend remains opposite as that of the rig data. As mentioned previously, LES with a flamelet model makes improvements to the prediction of the pattern factor

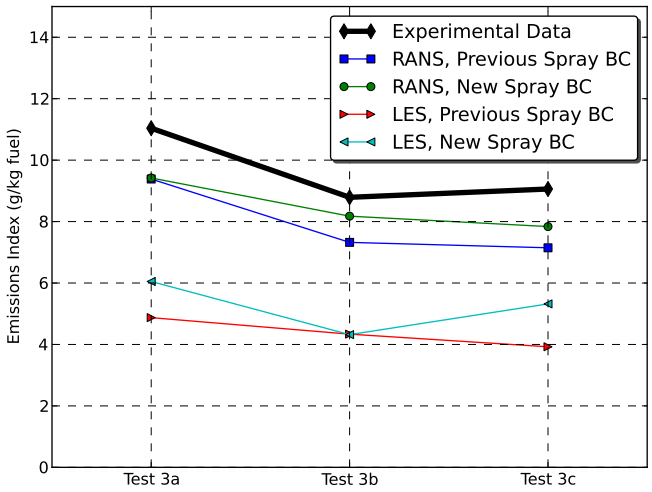

Figure 4.2: NO_x EI for both sets of fuel BC using the flamelet model.

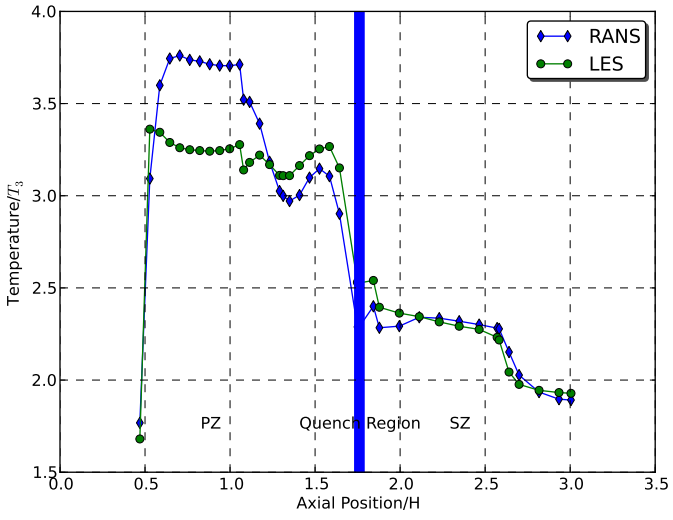

Figure 4.3: Average temperature on cross sections along the axis of combustor.

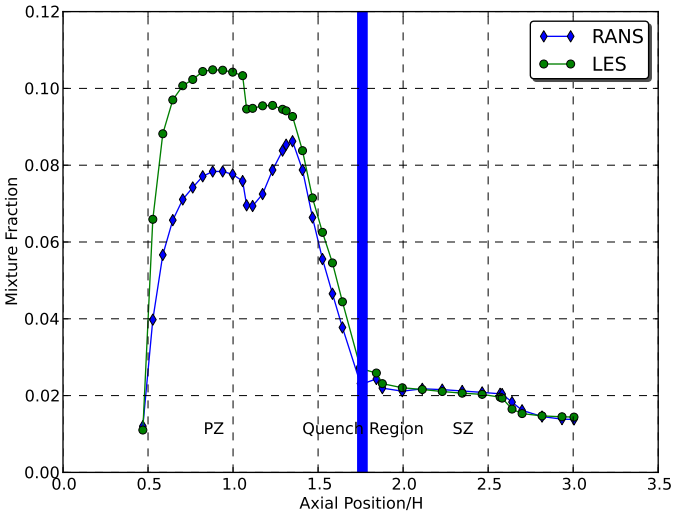

Figure 4.4: Average mixture fraction on cross sections along the axis of combustor.

and the new spray boundary conditions make further improvements to the trend in PF with this set of turbulence and chemistry models. With the new spray boundary conditions, the PF drops closer in value at the third configuration, however it is still larger than that of the second configuration.

Radial profiles for each configuration using all turbulence, chemistry, and atomization models are shown in Figure 4.7 - Figure 4.9. Among the figures, it is shown that in all RANS simulations, the radial profiles collapse onto one curve leading to the conclusion that for radial profile prediction, RANS is insensitive to the combustion model used or fuel boundary condition used. While in LES, decent improvement in the second configuration is made with the new spray model, however, the results slightly degraded in the first case. The radial profile in the third configuration remained mostly unaffected.

Exit temperature distributions are shown in Figure 4.10 - Figure 4.15. For ease of comparison, the previous data from the baseline simulations are shown. Similar

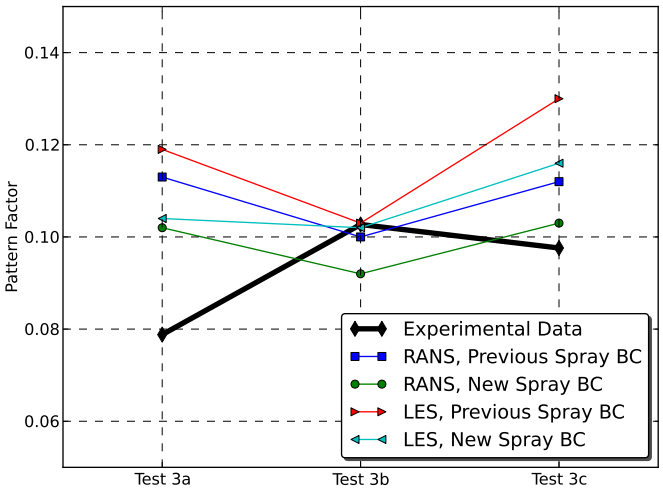

Figure 4.5: Pattern Factor for both sets of fuel BC using the equilibrium model.

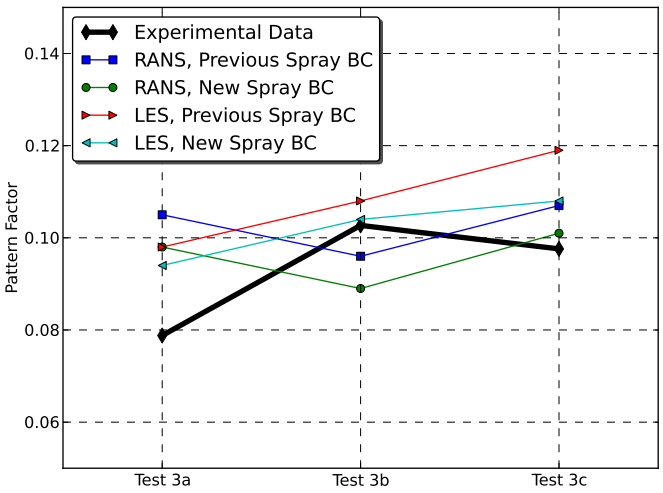

Figure 4.6: Pattern Factor for both sets of fuel BC using the flamelet model.

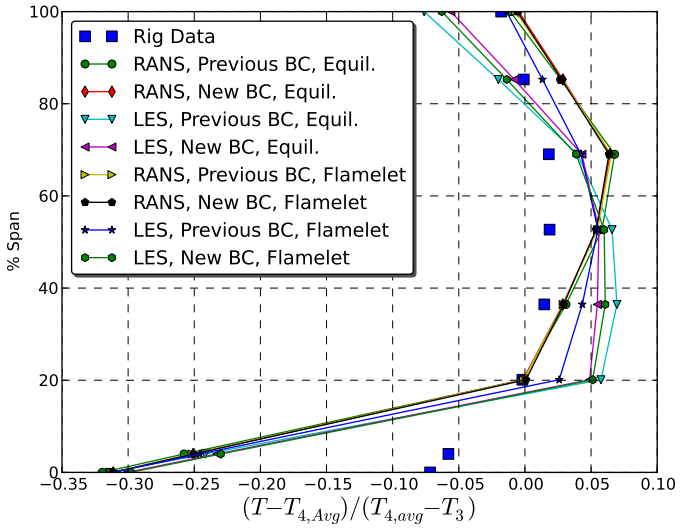

Figure 4.7: Radial temperature profile of Test 3a for both sets of fuel BC.

to radial temperature profile results, comparisons between the two spray boundary conditions using the RANS turbulence model show very small differences. With LES and the flamelet model, the results with the new atomization model show increases in the size of hot spots. With LES and the equilibrium model, the results using the new atomization model show the hot spots decreasing in size.

Lastly, an improvement to the NO_x trend is made through the use of a different set of liner wall boundary conditions. Recall that the boundary condition for the combustor liner was set as a temperature boundary condition where the temperature was found from rig data. The temperature boundary condition has been set the same for all configurations. The temperature of the liner is likely to vary among the configurations, influencing the value of NO_x formed. To allow the temperature of the liner to vary, an adiabatic boundary condition was used in a RANS simulation. As Figure 4.16 shows, this boundary condition accounts for the variation in liner

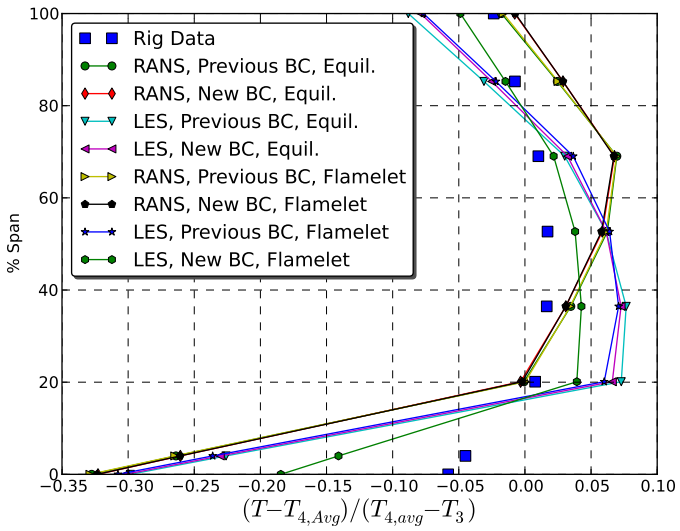

Figure 4.8: Radial temperature profile of Test 3b for both sets of fuel BC.

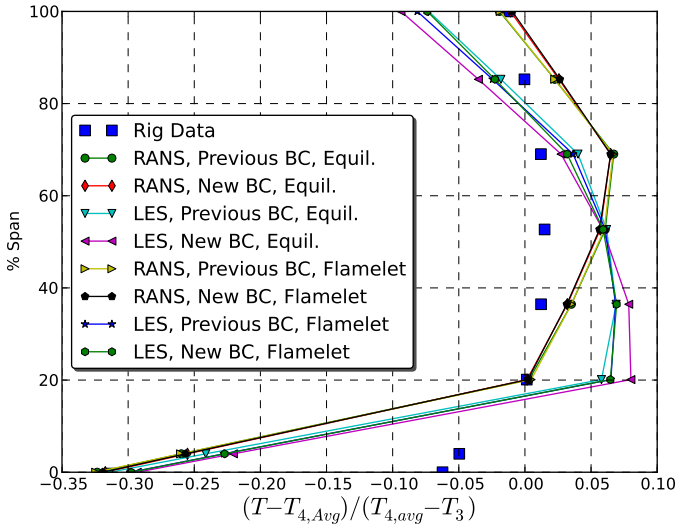

Figure 4.9: Radial temperature profile of Test 3c for both sets of fuel BC.

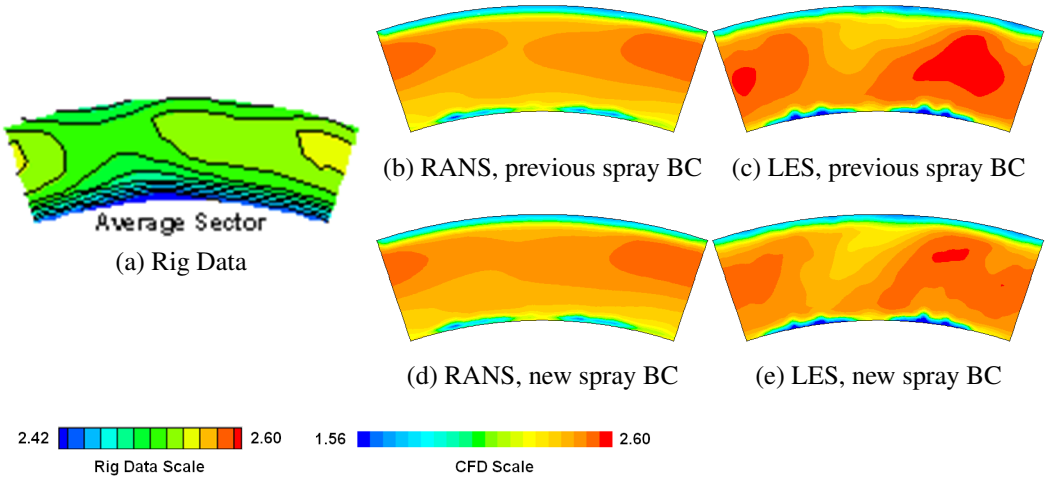

(a) Rig Data (b) RANS, previous spray BC (c) LES, previous spray BC

(d) RANS, new spray BC (e) LES, new spray BC

Figure 4.10: Exit temperature contours of Test 3a with equilibrium model.

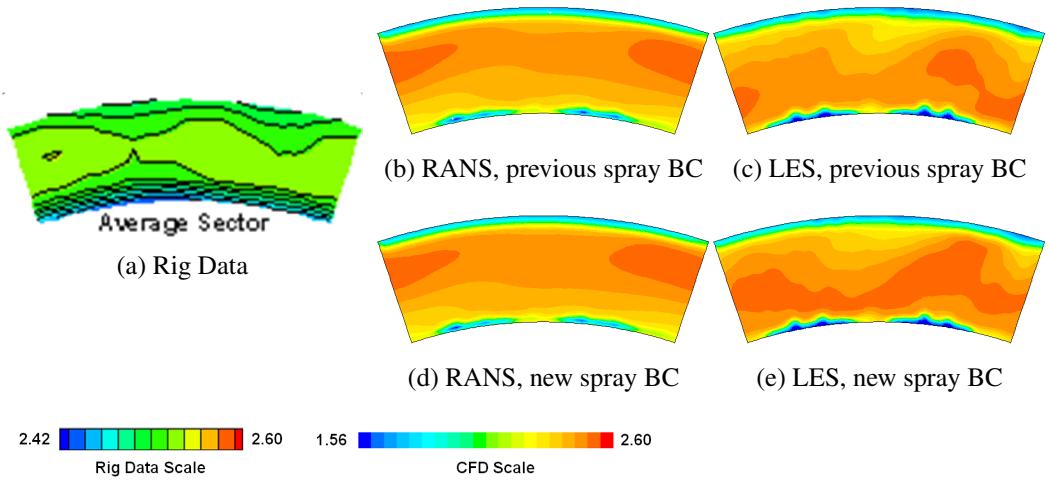

(a) Rig Data (b) RANS, previous spray BC (c) LES, previous spray BC

(d) RANS, new spray BC (e) LES, new spray BC

Figure 4.11: Exit temperature contours of Test 3b with equilibrium model.

temperature and predicts the trend in NO_x among the three configurations most consistently.

4.3 Conclusions

From these results, it is shown that the new, simpler spray model either improves upon or at minimum, matches the performance of the simulations using boundary conditions based upon experimental data. Little differences are observed when the

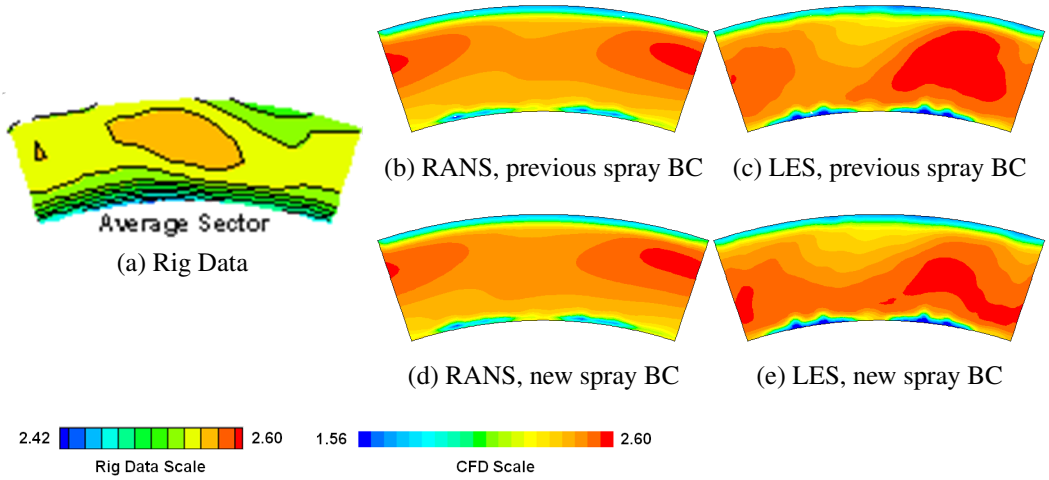

(a) Rig Data (b) RANS, previous spray BC (c) LES, previous spray BC (d) RANS, new spray BC (e) LES, new spray BC

Figure 4.12: Exit temperature contours of Test 3c with equilibrium model.

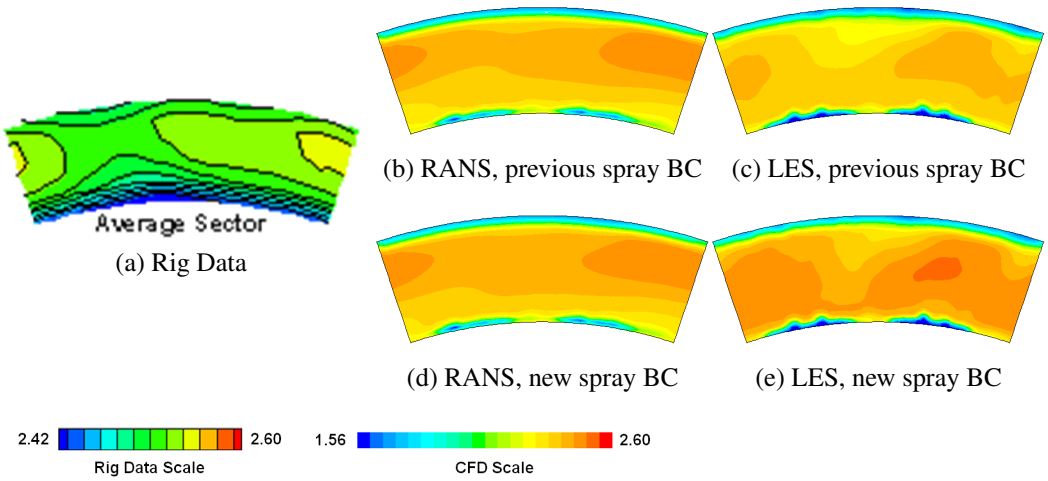

(a) Rig Data (b) RANS, previous spray BC (c) LES, previous spray BC (d) RANS, new spray BC (e) LES, new spray BC

Figure 4.13: Exit temperature contours of Test 3a with flamelet model.

spray model is used with RANS/equilibrium. The spray model has shown some improvement in pollutant predictions with RANS/flamelet. Although, still significantly under predicting NO_x concentrations, the LES/flamelet model predicted the correct trend in data. LES/flamelet also predicted PF most accurately. Finally, it was seen that it is essential to take into account variation in wall liner temperature to correctly predict NO_x trend among the configurations.

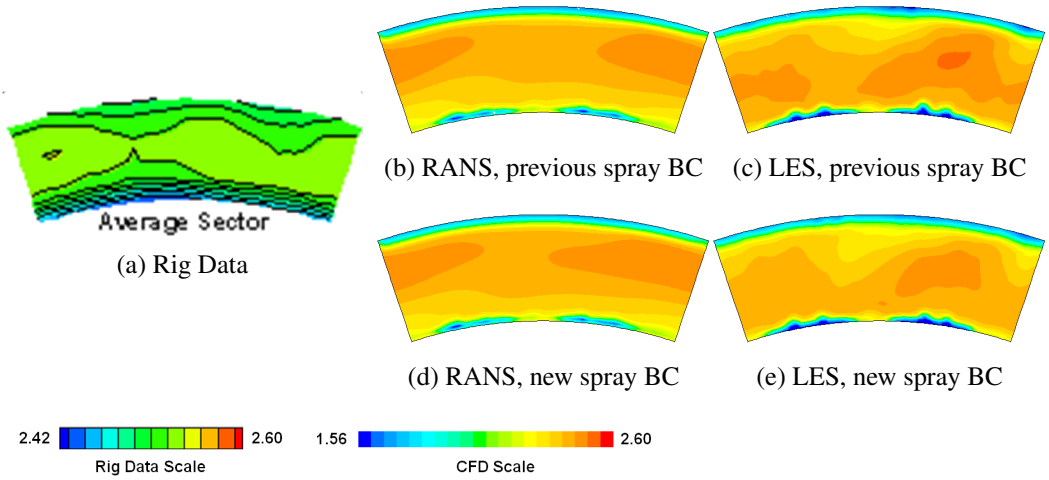

(a) Rig Data (b) RANS, previous spray BC (c) LES, previous spray BC

(d) RANS, new spray BC (e) LES, new spray BC

Figure 4.14: Exit temperature contours of Test 3b with flamelet model.

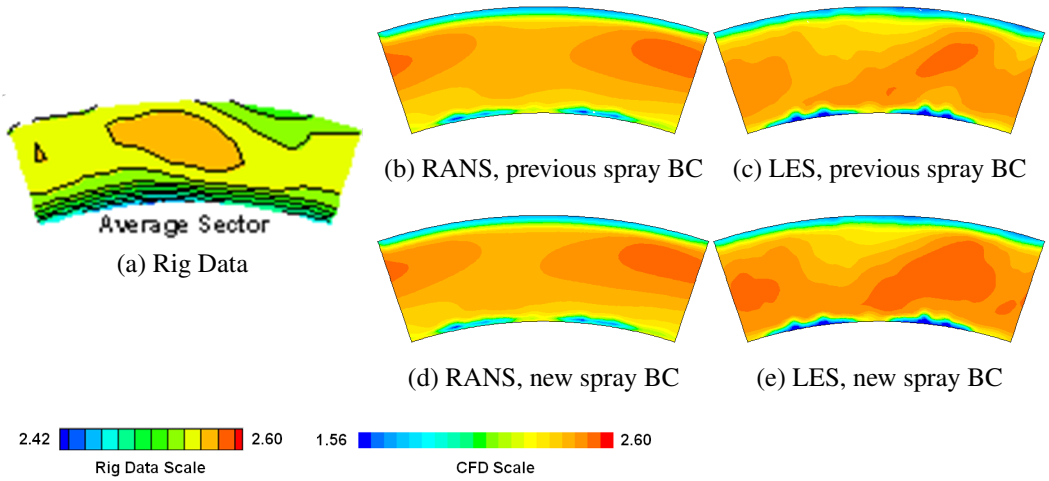

(a) Rig Data (b) RANS, previous spray BC (c) LES, previous spray BC

(d) RANS, new spray BC (e) LES, new spray BC

Figure 4.15: Exit temperature contours of Test 3c with flamelet model.

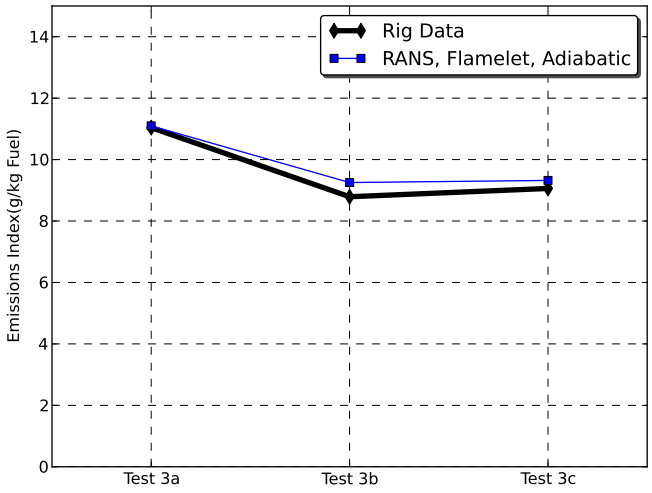

Figure 4.16: NO_x EI using an adiabatic boundary condition for the combustor liner.

Chapter 5

Predictive Study of a Series of Configurations

5.1 Introduction

To test the conclusions made in the study of the previous three configurations and to generalize these conclusions, a series of eight combustor configurations were simulated. The configurations varied by geometry differences such as swirlers, air dilution holes, and effusion cooling patterns. The details of the changes are not important since the objective is to evaluate the CFD model's performance, but the differences among the configurations is shown in Table 5.1.

Table 5.1: Changes among all configurations.

Test	Swirlers	Quench Holes	Effusion	Secondary Air		Comment
				Inner	Outer	
Test 3a	S3a	Q3abc	E3abc	None	SAO3abc	
Test 3b	S3b	Q3abc	E3abc	None	SAO3abc	
Test 3c	S3c	Q3abc	E3abc	None	SAO3abc	
T1	S3a	Q1	E1	SAI1	SAO1	
T2	S2	Q1	E1	SAI2	SAO2	
T3	S3a	Q1	E3	SAI1	SAO1	Primary zone changes
T4	S4	Q4	E4	SAI1	SAO1	
T5	S2	Q5	E5	SAI1	SAO1	
T6	S6	Q4	E4	SAI1	SAO1	Tangential inlet direction changed from previous
T7	S6	Q7	E4	SAI7	SAO7	Tangential inlet same as in T6
T8	S8	Q7	E4	SAI7	SAO7	Tangential inlet same as in T6

In the previous study, experimental data was given before hand and any tuning of the physical submodel's parameters or types of boundary conditions was per-

missible. For this new study simulations were performed first and only after the results were documented was experimental data obtained. Therefore, the CFD configuration considered to model the combustor most accurately from the previous simulations was set and used for these eight configurations, which constitutes a true blind validation test of the CFD method. The metrics that had been previously used for comparison between rig data and CFD data are again used here. Additionally, pressure drop measurements in the combustor were also compared. The combustors were meshed so that the cell counts were similar to that of the previous three configurations, approximately 12.5 million cells. However, due to the varying geometries of the combustors, the cell count ranged from 11.6 to 14.0 million cells. The equilibrium and flamelet model were run with a RANS turbulence model and to save computational time, only the equilibrium model was run in LES. As previously shown, for RANS, the equilibrium and flamelet model give very similar results for radial temperature profiles with the exception of having higher temperatures, the equilibrium model gives similar results as the flamelet model for exit temperature distributions. Therefore, the temperature distributions and profiles are only shown for the equilibrium model.

5.2 Results and Discussion

NO_x concentrations are shown in Figure 5.1. When using adiabatic liner walls for the previous study, results were shown to be almost identical in value for the previous three configurations, see Figure 4.16. In this study, however, rig data is bracketed between the flamelet and equilibrium models when using RANS. The results using the RANS/flamelet model are almost completely consistent with the rig data trend expect for the large decrease in NO_x concentration seen from T5 to T6 which the simulations do not capture. The equilibrium model is mostly consistent with the flamelet model's trend except for being lower in value. In LES, a slight

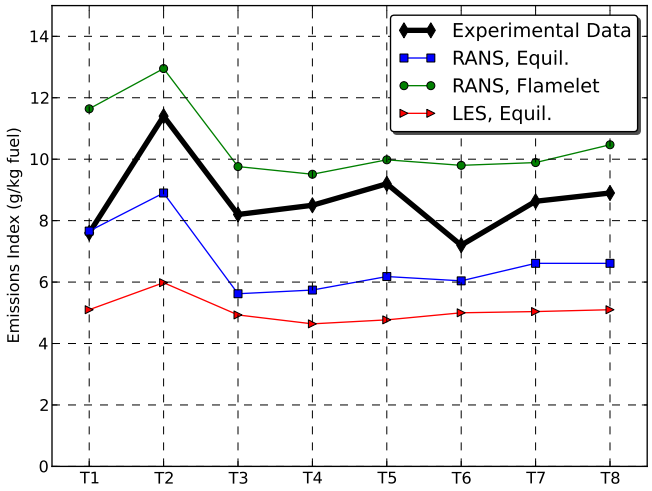

Figure 5.1: NO_x EI for predictive study of the eight configurations.

under prediction of NO_x is seen, with respect to the RANS equilibrium values. Also, notice the minimum and maximum values are not as pronounced as they are with the RANS turbulence model.

Next, pattern factors at the exit are compared to rig data for all configurations which is shown in Figure 5.2. In RANS, the pattern factor is predicted extremely poorly. The pattern factor is significantly over predicted and the trend is not consistent with the rig data. However with the LES turbulence model, it is seen that the pattern factor trend is predicted quite well. LES does considerably over predict PF for T3 and T5. It should be reiterated that in the previous study the most consistent results for pattern factor used the LES/flamelet model. Therefore, it may be possible to achieve better results using the LES/flamelet model for these configurations.

In Figure 5.3 - Figure 5.10 exit temperature distributions are shown. Here it is shown why pattern factors for the RANS simulations were over predicted to such a great extent. In the RANS simulations there are regions of unevenly mixed gases

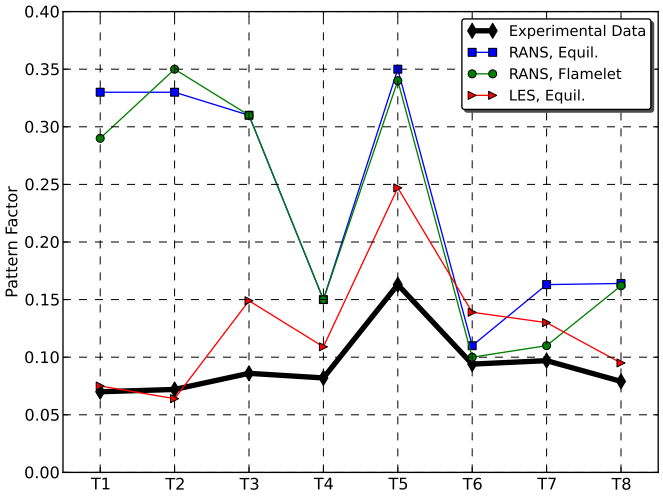

Figure 5.2: Pattern Factor for predictive study of the eight configurations.

at the exit. In LES, the exit temperature is much more uniform, as also seen in rig data. In T3, T5, T6, T7, and T8, locations and patterns of hot spots are also correctly predicted with LES.

After looking at exit temperature distributions it is expected that LES will predict radial temperature profiles better which are shown in Figure 5.11 - Figure 5.18. Peak temperatures are greatly over predicted for most of the results obtained from the RANS model and the results from the LES model show a much flatter, uniform exit temperature. Again, in all of these radial temperature profiles, a significant under prediction of temperature is seen at the hub of the exit.

Additionally, the total pressure drop across the combustor as well as the pressure drops at three positions in the annulus from the simulations were compared to those from rig data. Figure 5.19 shows the total pressure across the combustor and Figure 5.20 shows the pressure at the outer, dome, and inner annulus. The pressure in the annuli were averaged over axial cross sections at the axial location the

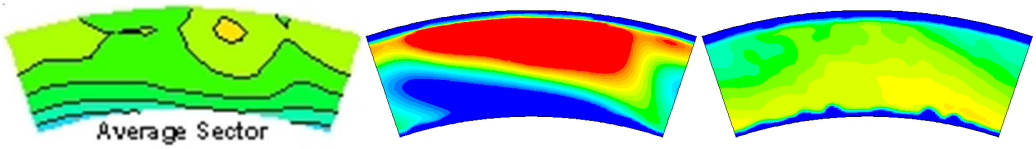

(a) Rig Data (b) RANS Turbulence Model (c) LES Turbulence Model

Figure 5.3: Exit temperature contours of T1 with equilibrium model.

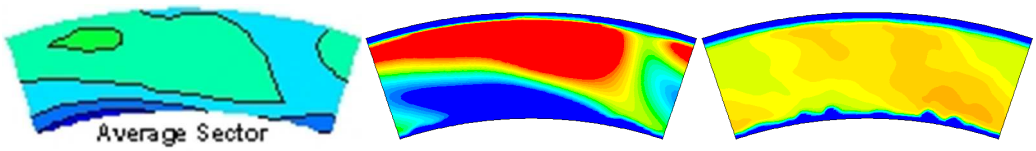

(a) Rig Data (b) RANS Turbulence Model (c) LES Turbulence Model

Figure 5.4: Exit temperature contours of T2 with equilibrium model.

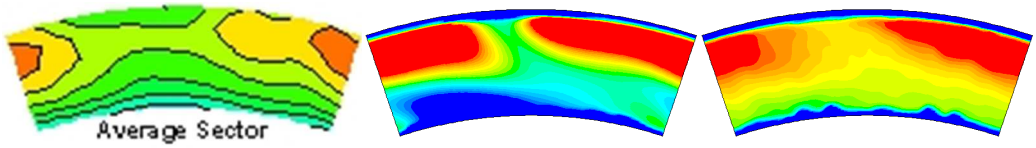

(a) Rig Data (b) RANS Turbulence Model (c) LES Turbulence Model

Figure 5.5: Exit temperature contours of T3 with equilibrium model.

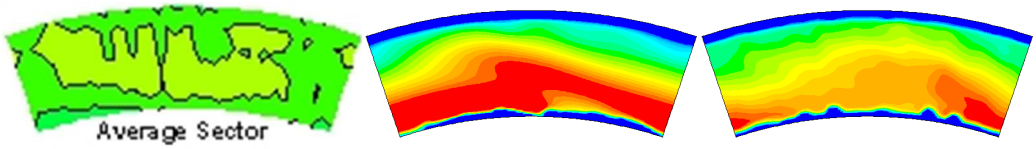

(a) Rig Data (b) RANS Turbulence Model (c) LES Turbulence Model

Figure 5.6: Exit temperature contours of T4 with equilibrium model.

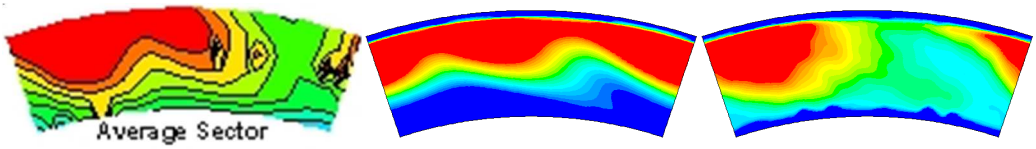

(a) Rig Data (b) RANS Turbulence Model (c) LES Turbulence Model

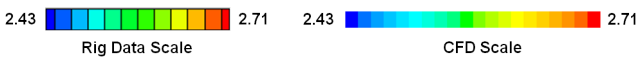

Figure 5.7: Exit temperature contours of T5 with equilibrium model.

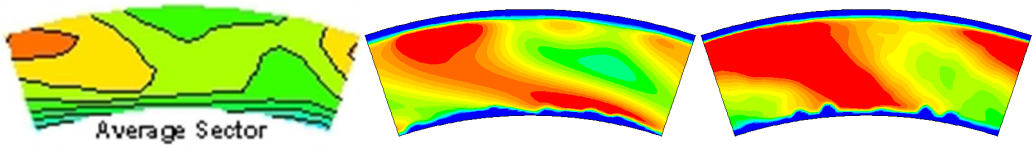

(a) Rig Data (b) RANS Turbulence Model (c) LES Turbulence Model

Figure 5.8: Exit temperature contours of T6 with equilibrium model.

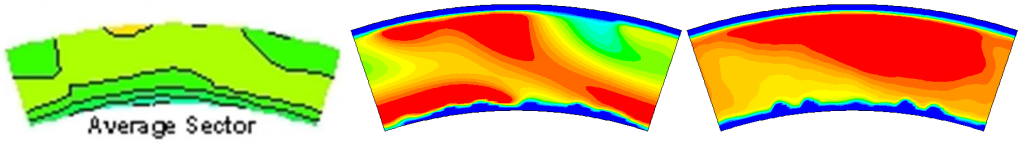

(a) Rig Data (b) RANS Turbulence Model (c) LES Turbulence Model

Figure 5.9: Exit temperature contours of T7 with equilibrium model.

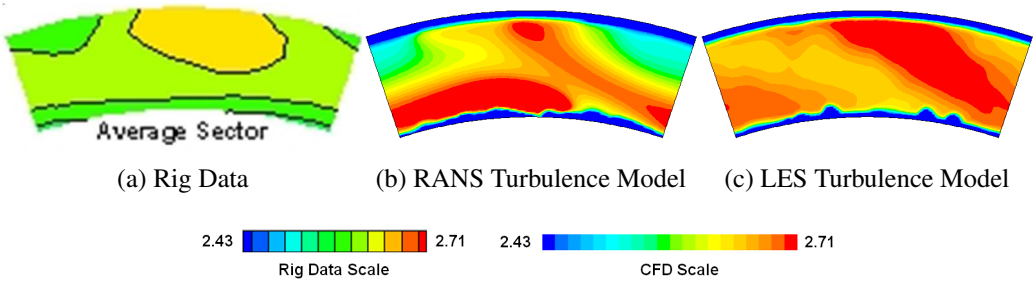

(a) Rig Data (b) RANS Turbulence Model (c) LES Turbulence Model

Figure 5.10: Exit temperature contours of T8 with equilibrium model.

pressure was taken on the rig. Although the trend is reasonably well predicted, the pressure in the annulus is consistently higher in the CFD results. This is due to inaccuracy in the pressure drop across the liner and most likely due to the error using non-conformal mesh. The results using LES are closer to the experimental data at all locations the pressure was measured at.

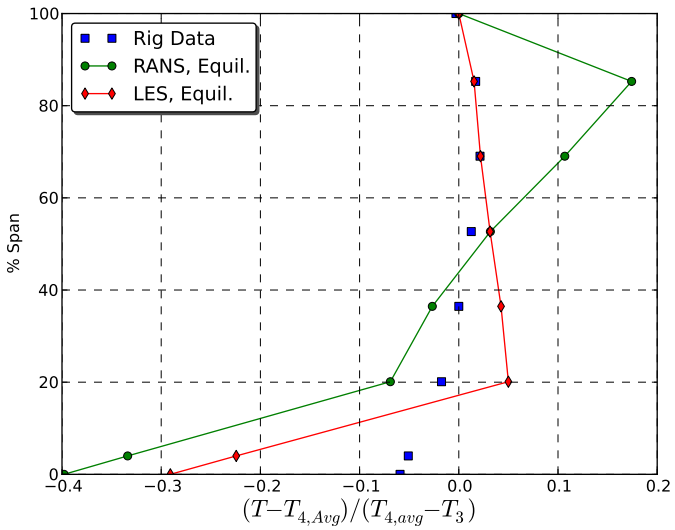

Figure 5.11: Radial temperature profile for T1.

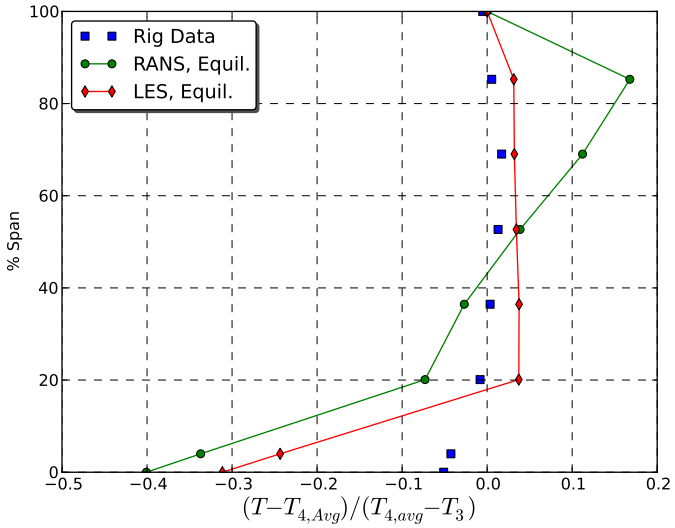

Figure 5.12: Radial temperature profile for T2.

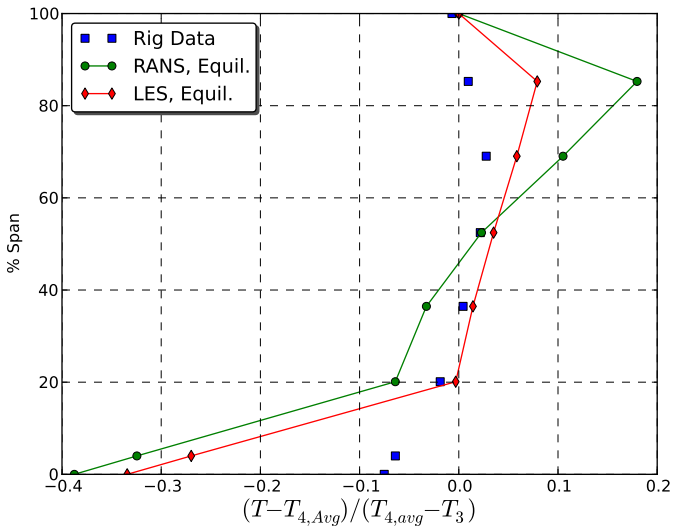

Figure 5.13: Radial temperature profile for T3.

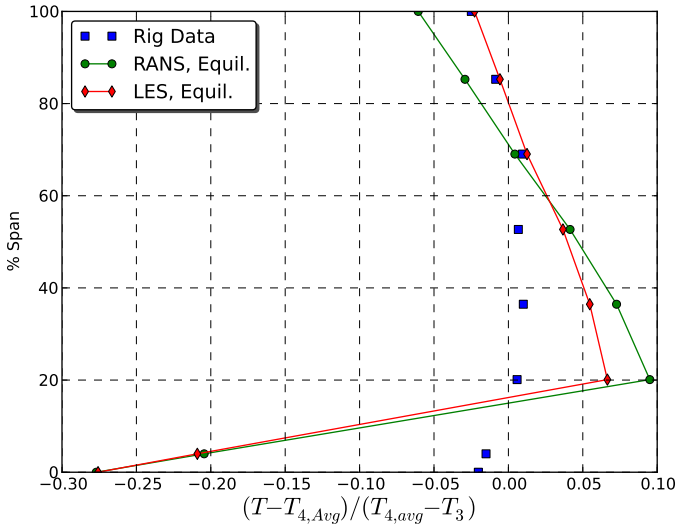

Figure 5.14: Radial temperature profile for T4.

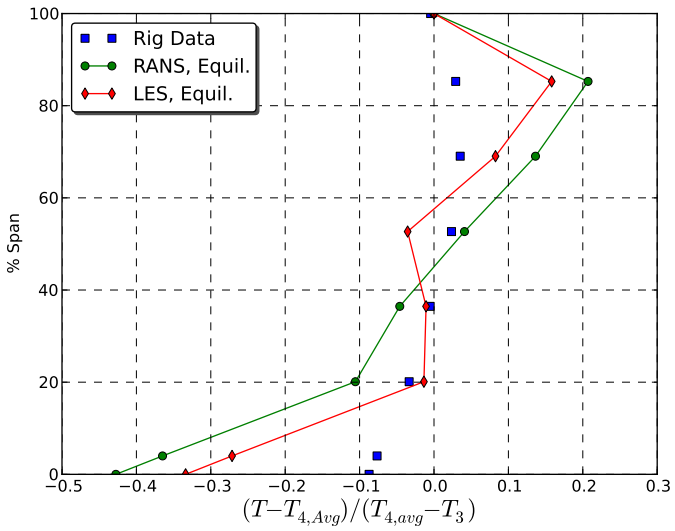

Figure 5.15: Radial temperature profile for T5.

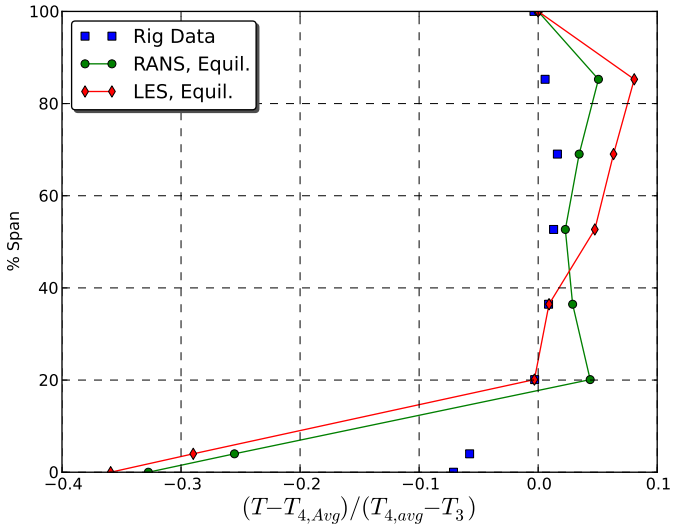

Figure 5.16: Radial temperature profile for T6.

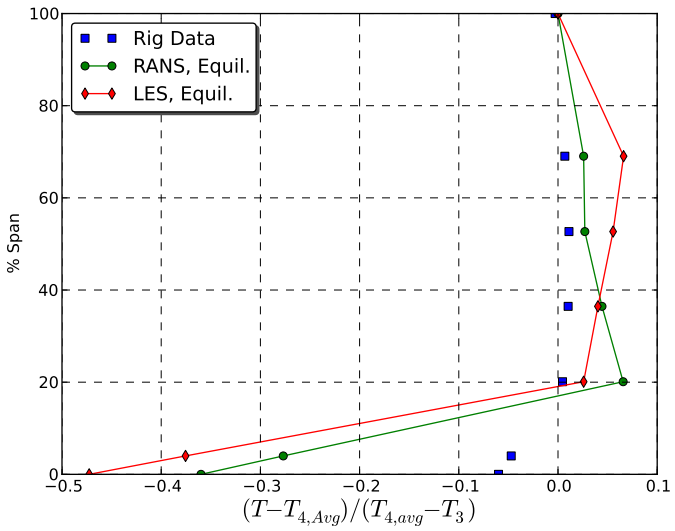

Figure 5.17: Radial temperature profile for T7.

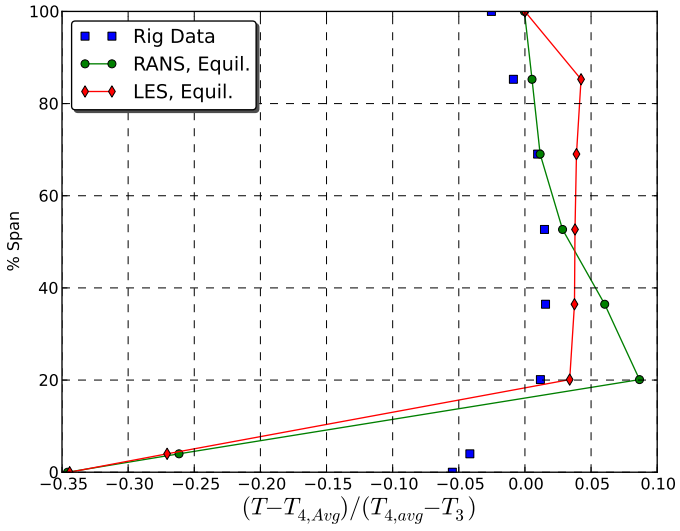

Figure 5.18: Radial temperature profile for T8.

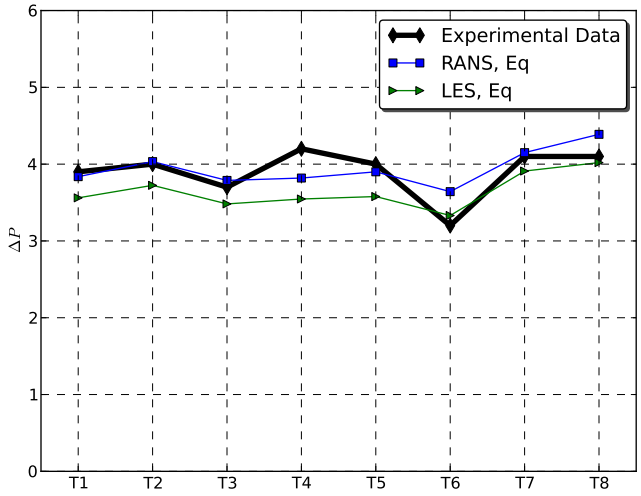

Figure 5.19: Total pressure drop across the combustor.

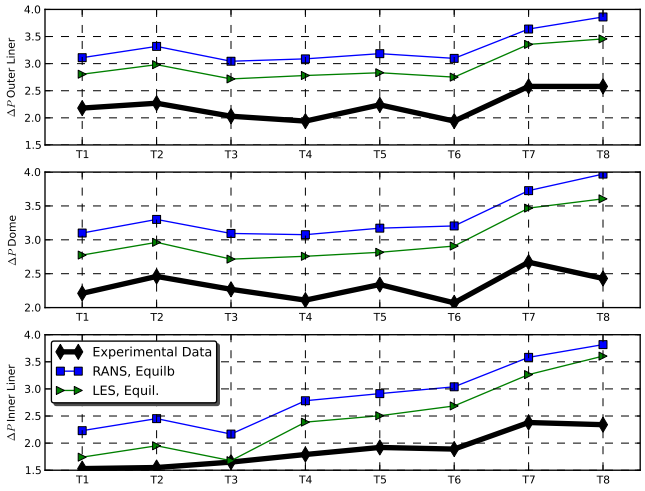

Figure 5.20: Pressure drops for the outer annulus, dome annulus, and inner annulus.

Chapter 6

Mesh Refinement Study

6.1 Introduction

The last part of this work looked at mesh resolution to see if any of the error between numerical simulations and experimental data can be due to inadequate mesh resolution. Increases in computational resources in the last decade have allowed for mesh resolution studies in complex, reacting flow configurations [25]. The previous simulations were limited in some sense that mesh resolution was desired to be kept at a level practical for applications in industry where turnaround time of simulations is important while still having meaningful results. Once a mesh has been refined sufficiently for RANS simulations, results should be independent of the mesh. In LES, there will never be a point at which the results will be mesh independent, however, time averaged quantities must converge for stationary flows.

For this study, the previous 12.5 million cell grid was manually coarsened to a mesh size of approximately 5 million cells. By splitting each cell into 8, this coarse mesh was then refined using ANSYS FLUENT to approximately 40 million cells. Therefore, this study will compare three mesh counts: 5, 12.5, and 40 million cells which will be referred to as the coarse, baseline, and fine mesh, respectively. Additionally, the coarse mesh was refined on only wall adjacent cells to keep the same y^+ as the fine mesh which will be referred to as the coarse/fine wall mesh. The configuration used was T8. The same physical models used in Chapter 5 were used for this study except the flamelet model was not used here.

6.2 Results and Discussion

Using temperature distributions on the center plane, one is able to compare the flow patterns using different mesh counts. First, the results from the RANS simulations in Figure 6.1 - Figure 6.3 will be discussed. The coarse and baseline mesh show

nearly identical temperature distributions. The temperature in the center of the primary zone decreases slightly in the coarse mesh with respect to the baseline mesh but all the dilution air patterns are consistent in both meshes. In the fine mesh, it is noticed that the coldest spot in the primary zone shifts down. The secondary zone after the mixing region also appears to be slightly cooler.

Figure 6.4 - Figure 6.6 show the results using the LES turbulence model. There are some obvious differences among all three cases. As the mesh is refined the colder spot in the center of the primary zone decreases and overall, the primary zone increases in temperature. The increase in temperature, however, did not increase the levels of NO_x concentrations.

Comparing exit temperature distributions, one is able to see that as the mesh is refined, the temperature decreases and converges to a pattern closer to the rig data. The rig data temperature distribution from Figure 5.10a is repeated below the CFD data for ease of comparison. In RANS, the temperature of the lower hot spot decreases, which is not present in the rig data and in LES, although the temperature of the hot spot is still slightly over predicted, the temperature distribution is well represented. To investigate whether this may be purely an issue of mixing close to the wall, cells adjacent to the wall in the coarse mesh were refined. Therefore, y^+ values remained the same for each mesh. Figure 6.9, shows that the exit temperature distribution fits in-between the baseline and fine mesh for the RANS turbulence model but wall refinement did not affect the results to such a great extent in LES.

The radial temperature profile is shown in Figure 6.7. As pointed out before, the previous simulations showed a very cold region along the bottom of the exit of the combustor which can be attributed to inaccurate modeling of the mixing of the wall cooling and hot gases at the exit. Once the mesh is refined, the simulations then capture the profile at the bottom of the combustor exit. It was thought that this may

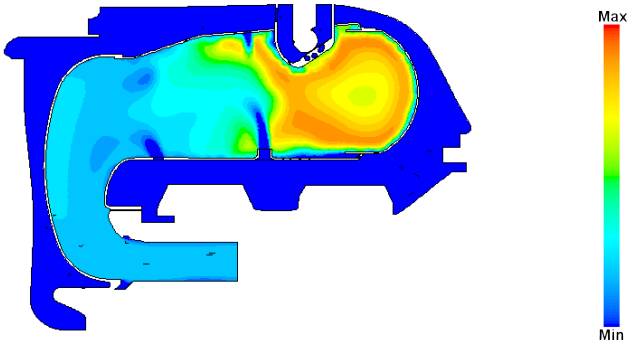

Figure 6.1: Temperature distribution on center plane for coarse mesh using the RANS turbulence model.

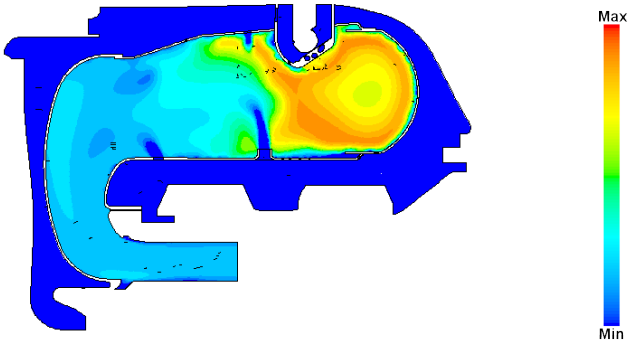

Figure 6.2: Temperature distribution on center plane for baseline mesh using the RANS turbulence model.

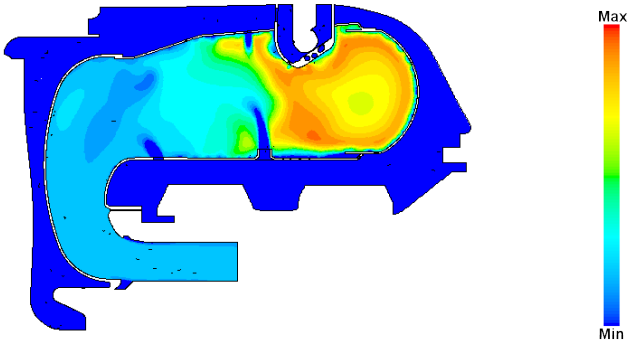

Figure 6.3: Temperature distribution on center plane for fine mesh using the RANS turbulence model.

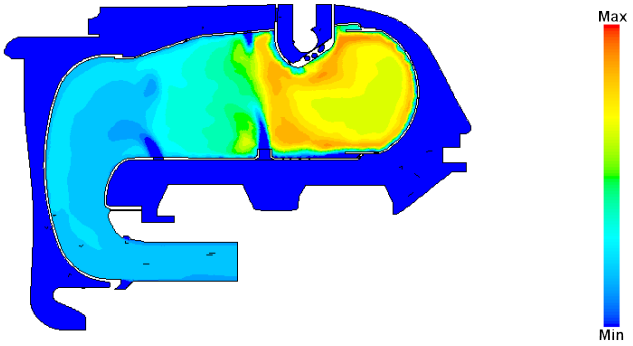

Figure 6.4: Temperature distribution on center plane for coarse mesh using the LES turbulence model.

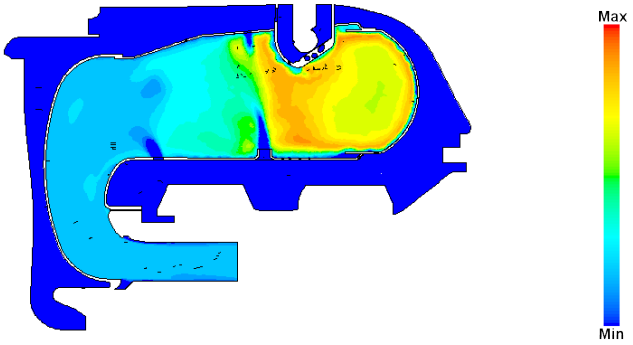

Figure 6.5: Temperature distribution on center plane for baseline mesh using the LES turbulence model.

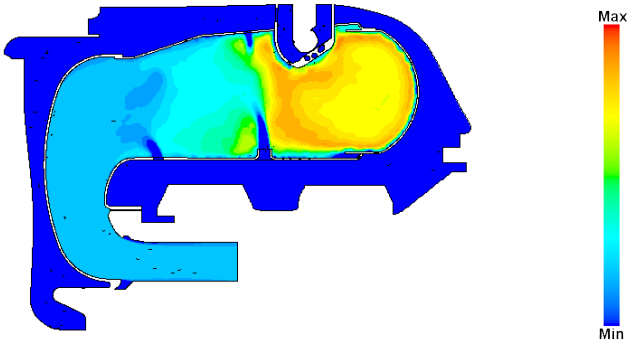

Figure 6.6: Temperature distribution on center plane for fine mesh using the LES turbulence model.

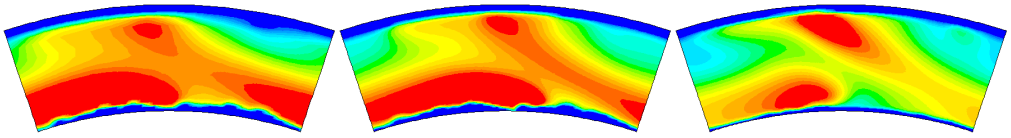

(a) Coarse (b) Baseline (c) Fine

Figure 6.7: Exit temperature contours for the refinement study using the RANS turbulence model.

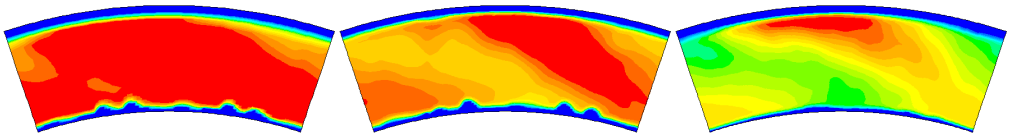

(a) Coarse (b) Baseline (c) Fine

Figure 6.8: Exit temperature contours for the refinement study using the RANS turbulence model.

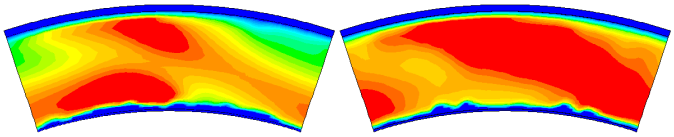

(a) RANS (b) LES

Figure 6.9: Refinement of wall adjacent cells only.

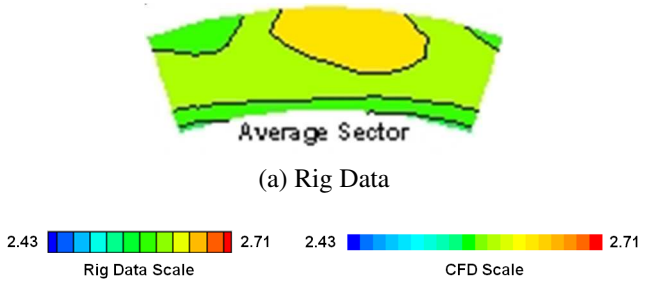

(a) Rig Data

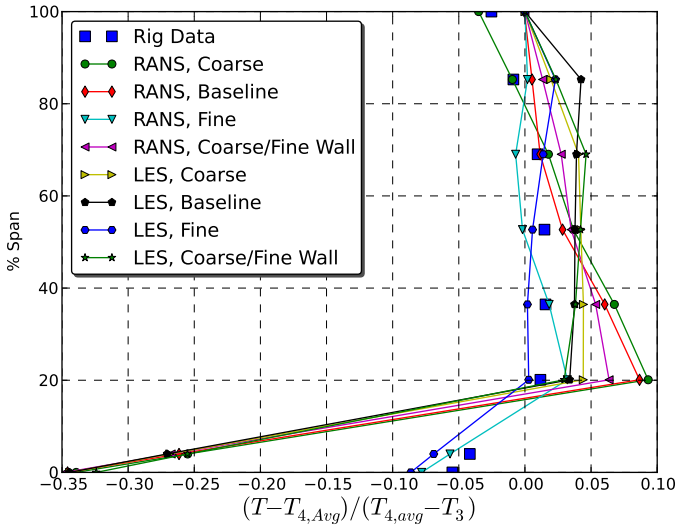

Figure 6.10: Radial temperature profile for the refinement study.

be due to inadequate resolution at the walls, however refining the cells adjacent to the wall to keep the same y^+ as the fine mesh does not show the same profile near the hub.

Chapter 7

Conclusions

Large Eddy Simulations have potential to improve computational modeling of complex, reacting flows such as those found in gas turbine combustors. LES is still being developed for uses in industry applications and in a lot of industries RANS turbulence models are still primarily relied upon. This work has explored the use of LES in a complex, real world, gas turbine combustor. As a result of this work, more insight in the application of not only LES but also in general simulations of this combustor has been obtained.

In the fuel spray modeling study, it was shown that LES is necessary to correctly characterize the additional breakup of the fuel spray caused by the air shrouds. Using the stochastic breakup model, the overall SMDs at the 1.00" plane were reasonably close in value to those given in the experiment and the trend across the three shroud configurations was also reasonably consistent with the experimental data. The result of this study was a fuel spray model that was used in simulations of the gas turbine combustor. For the specified operating condition, the boundary conditions only require knowledge of a diameter distribution of the atomizer alone. These fuel boundary conditions can be used without changes for any shroud configuration. This change alone cuts time from having to prototype shroud geometries and conduct experimental spray testing in order to have the correct diameter distribution for combustor simulations.

The baseline combustor simulations use an experimentally measured diameter distribution for every shroud configuration. The results of these simulations were compared to combustor simulations using the new, simpler fuel spray model. Results using the new spray model were shown in most cases to improve upon or at

minimum match the baseline simulations. Additionally, eight combustor configurations were simulated with the new fuel spray model in a blind validation study. Overall, it can be seen that the new spray model along with the RANS turbulence model and flamelet model, is able to reasonably predict the NO_x concentration trend across a set of configurations without the need of an input diameter distribution specific to the swirler geometry. In LES, NO_x was under predicted due to lower temperatures seen in the primary zone which obscures improvements made with the new spray model. Further work looking into the cause of the lower temperature of the primary zone using LES should be performed. Relying on the LES turbulence model's ability to predict mixing better, temperature metrics at the exit of the combustor, which include temperature distribution, profile, and pattern factor, are all shown to be better predicted with the LES turbulence model.

It was also discovered that inadequate mesh resolution of the combustor was causing mixing of exit wall cooling to be inaccurately described. Increasing the level of resolution greatly improved the correlation between rig data and computer simulations. The mesh count used in the fine mesh may not be practical for quick turnaround times in industry with current computer resources. Increasing the amount of computational resources would be needed to use this amount of resolution as part of the design process.

Further investigation should be looked into resolving the issue of the lower values of NO_x seen in LES. It was shown that the mixture fraction distribution in the primary zone in RANS and LES were quite different and thus the temperature distribution in the primary zone was also different. Mesh refinement did help to reduce the difference in temperature between the two models but did not increase NO_x concentration in LES. If this issue can be resolved without adversely affect-

ing other comparison metrics, the CFD method using LES would be shown to be superior to RANS on all metrics of comparison used in this work.

REFERENCES

[1] A. Lefebvre and D. Ballal, *Gas Turbine Combustion—Alternative Fuels and Emissions,* Third Edition. CRC Press, 2010.

[2] A. Lefebvre, *Atomization and Sprays*. Hemisphere Publishing Corporation, 1989.

[3] P. Rosin and E. Rammler, "The laws governing the fineness of powdered coal," *Journal of the Institute of Fuel*, vol. 7, pp. 29–36, 1933.

[4] P. Bernard, *Turbulent Flow: Analysis, Measurement and Prediction*. Wiley, 2002.

[5] B. Launder and N. Sandham, *Closure Strategies for Turbulent and Transitional Flows*. Cambridge University Press, 2001.

[6] T. Poinsot and D. Veynante, *Theoretical and Numerical Combustion*, Second Edition. R.T. Edwards, Inc., 2005.

[7] T. Shih, W. Liou, A. Shabbir, Z. Yang, and J. Zhu, "A new $\kappa-\varepsilon$ eddy viscosity model for high reynolds number turbulent flows," *Computers & Fluids*, vol. 24, no. 3, pp. 227 –238, 1995.

[8] J. Smagorinsky, "General circulation experiments with the primative equations," *Monthly Weather Review*, vol. 91, no. 3, 1963.

[9] M. Lesieur and O. Metais, "New trends in large-eddy simulations of turbulence," *Annual Review of Fluid Mechanics*, vol. 28, no. 1, pp. 45–82, 1996.

[10] M. Germano, U. Piomelli, P. Moin, and W. Cabot, "A dynamic subgrid-scale eddy viscosity model," *Physics of Fluids*, vol. 3, no. 7, 1991.

[11] N. Peters, *Turbulent Combustion*. Cambridge University Press, 2000.

[12] H. Pitsch, H. Barths, and N. Peters, "Three-dimensional modeling of nox and soot formation in di-diesel engines using detailed chemistry based on the interactive flamelet approach," *SAE Paper 962057*, 1996.

[13] C. Pierce and P. Moin, "A dynamic model for subgrid-scale variance and dissipation rate of a conserved scalar," *Physics of Fluids*, vol. 10, no. 12, 1998.

[14] N. Ashgriz, *Handbook of Atomization and Sprays: Theory and Applications*. Springer, 2011.

[15] C. Bowman, "Kinetics of pollutant formation and destruction in combustion," *Progress in Energy and Combustion Science*, vol. 1, no. 1, pp. 33–45, 1975.

[16] W. Gardiner, *Combustion Chemistry*. Springer-Verlag, 1984.

[17] A. Westenberg, "Kinetics of no and co in lean, premixed hydrocarbon-air flames," *Combustion Science and Technology*, vol. 4, no. 1, pp. 59–64, 1971.

[18] ANSYS, 2009, FLUENT Theory Guide.

[19] R. Reitz, "Modeling atomization processes in high-pressure vaporizing sprays," *Atomization and Spray Technology*, vol. 3, no. 4, pp. 309 –337, 1987.

[20] M. Lai, W. Freeman, P. Yankowich, J. Bryant, and P. Walterscheid, "High pressure spray diagnostics facility for development and evaluation of aero-engine atomizer and swirler assemblies," *ASME Conference Proceedings*, vol. 2004, no. 41669, pp. 665–671, 2004.

[21] D. Schmidt, I. Nouar, P. Senecal, J. Hoffman, C. Rutland, J. Martin, and R. Reitz, "Pressure-swirl atomization in the near field," *SAE Paper 1999-01-0496*, 1999.

[22] P. Orouke and A. Amsden, "The tab method for numerical calculations of spray droplet breakup," *SAE Paper 872089*, 1987.

[23] S. Apte, M. Gorokhovski, and P. Moin, "Les of atomizing spray with stochastic modeling of secondary breakup," *Intl J. Multiphase Flow*, vol. 29, no. 9, pp. 1503 –1522, 2003.

[24] S. Apte, K. Mahesh, M. Gorokhovski, and P. Moin, "Stochastic modeling of atomizing spray in a complex swirl injector using large eddy simulation," *Proceedings of the Combustion Institute*, vol. 32, no. 2, pp. 2257 –2266, 2009.

[25] G. Boudier, L. Gicquel, and T. Poinsot, "Effects of mesh resolution on large eddy simulation of reacting flows in complex geometry combustors," *Combustion and Flame*, vol. 155, pp. 196–214, 2008.